Solar Phys (2016) 291:3385–3426
DOI 10.1007/s11207-016-0981-3



# Spatio-temporal Dynamics of Sources of Hard X-Ray Pulsations in Solar Flares

**S.A. Kuznetsov[1,2,3] · I.V. Zimovets[3,4,5,2] · A.S. Morgachev[1,2] · A.B. Struminsky[3,6]**

Received: 14 February 2016 / Accepted: 20 August 2016 / Published online: 14 September 2016


**Abstract** We present a systematic analysis of the spatio-temporal evolution of sources of hard X-ray (HXR) pulsations in solar flares. We concentrate on disk flares whose impulsive phases are accompanied by a series of more than three successive peaks (pulsations) of HXR emission detected in the RHESSI 50 – 100 keV energy channel with a four-second time cadence. Twenty-nine such flares observed from February 2002 to June 2015 with characteristic time differences between successive peaks $P \approx 8-270$ s are studied. The main observational result of the analysis is that sources of HXR pulsations in all flares are not stationary, they demonstrate apparent movements or displacements in the parent active regions from pulsation to pulsation. The flares can be subdivided into two main groups depending on the character of the dynamics of the HXR sources. Group 1 consists of 16 flares (55 %) that show systematic dynamics of the HXR sources from pulsation to pulsation with respect to a magnetic polarity inversion line (MPIL), which has a simple extended trace on the photosphere. Group 2 consists of 13 flares (45 %) that show more chaotic displacements of the HXR sources with respect to an MPIL with a more complex structure, and sometimes sev-

Waves in the Solar Corona: From Microphysics to Macrophysics
Guest Editors: Valery M. Nakariakov, David J. Pascoe, and Robert A. Sych

✉ I.V. Zimovets
ivanzim@iki.rssi.ru

1 Radiophysical Research Institute (NIRFI), Bolshaya Pecherskaya str. 25/12a, Nizhny Novgorod 603950, Russia

2 Central Astronomical Observatory at Pulkovo of the Russian Academy of Sciences, Pulkovskoye chaussee 65/1, Saint-Petersburg 196140, Russia

3 Space Research Institute (IKI) of the Russian Academy of Sciences, Profsoyuznaya str. 84/32, Moscow 117997, Russia

4 State Key Laboratory of Space Weather (SKSW), National Space Science Center (NSSC) of the Chinese Academy of Sciences, No. 1 Nanertiao, Zhongguancun, Haidian District, Beijing 100190, China

5 International Space Science Institute – Beijing (ISSI-BJ), No. 1 Nanertiao, Zhongguancun, Haidian District, Beijing 100190, China

6 Moscow Institute of Physics and Technology (State University), Institutskyi per. 9, Dolgoprudny, Moscow Region 141700, Russia

eral MPILs are present in the parent active regions of such flares. Based on the observations, we conclude that the mechanism of the flare HXR pulsations (at least with time differences of the considered range) is related to successive triggering of the flare energy release process in different magnetic loops (or bundles of loops) of the parent active regions. Group 1 flare regions consist of loops stacked into magnetic arcades that are extended along MPILs. Group 2 flare regions have more complex magnetic structures, and the loops are arranged more chaotically and randomly there. We also found that at least 14 (88 %) group 1 flares and 11 (85 %) group 2 flares are accompanied by coronal mass ejections (CMEs), *i.e.* the absolute majority of the flares we studied are eruptive events. This gives a strong indication that eruptive processes play an important role in the generation of HXR pulsations in flares. We suggest that an erupting flux rope can act as a trigger of the flare energy release. Its successive interaction with different loops of a parent active region can lead to apparent motion of HXR sources and to a series of HXR pulsations. However, the exact mechanism responsible for generating the pulsations remains unclear and requires a more detailed investigation.

**Keywords** Flares, dynamics · Flares, impulsive phase · Flares, relation to magnetic field · X-Ray bursts, hard

## 1. Introduction

One of the main properties of solar flares is their non-stationarity and the irregularity (intermittency) of their energy release processes in time. In particular, the light curves of hard X-ray (HXR) and microwave emission of many flares are composed of correlated sequences of peaks (bursts, pulses) with durations ranging from tens of milliseconds to a few minutes (Dennis, 1988; Aschwanden, 2002; White *et al.*, 2011). This indicates that electrons are accelerated in a series of many individual episodes of short duration with respect to the total duration of a flare, which can reach several hours. Perhaps an even more interesting phenomenon related to flares is the quasi-periodic character of HXR and microwave emission observed in some events (see, *e.g.*, Aschwanden, 1987; Dennis, 1988; Nakariakov and Melnikov, 2009; and references therein). In these cases, the time intervals between successive peaks (pulses or pulsations) of flare emission do not differ much from each other, and by extension, the Fourier or wavelet spectra of the emission time profiles contain significant peaks. We would like to emphasize here that this definition of the quasi-periodicity of pulsations is quite intuitive and not strict. To the best of our knowledge, there is no strict generally accepted definition of quasi-periodic pulsations (QPPs) of solar flare emission (see discussions, *e.g.*, in Aschwanden *et al.*, 1998; McAteer *et al.*, 2007; Nakariakov *et al.*, 2010; Gruber *et al.*, 2011; Inglis, Ireland, and Dominique, 2015).

Quasi-periodic pulsations (QPPs) in HXR and microwave emissions can represent special properties of the flare energy release, in particular, some specific regimes of magnetic reconnection (*e.g.*, Tajima *et al.*, 1987; Kliem, Karlický, and Benz, 2000; Ofman and Sui, 2006; Artemyev and Zimovets, 2012; McLaughlin, Thurgood, and MacTaggart, 2012; Li, Ning, and Zhang, 2015; Li and Zhang, 2015). QPPs can also be a result of a flare energy release modulated by some external quasi-periodic sources, such as oscillating coronal loops or sunspots located in a flare region or in close proximity (*e.g.*, Brown and Hoyng, 1975; Zaitsev and Stepanov, 1982; Foullon *et al.*, 2005; Nakariakov *et al.*, 2006; Sych *et al.*, 2009; Jakimiec and Tomczak, 2013, 2014). A scenario similar to a domino effect is also possible, when one episode of a flare energy release causes another episode of energy release, which

in turn causes another, and so on (Emslie, 1981; Nakariakov and Zimovets, 2011; Hood *et al.*, 2016). However, the physical mechanisms responsible for QPPs are an open question and a matter of active debate. A better understanding of these mechanisms is important for our general understanding of solar and stellar flares. Moreover, any good and reliable flare model must be able to explain the QPP phenomenon in a natural way.

A number of models were proposed to explain flare QPPs (see, *e.g.*, Aschwanden, 1987; Zaitsev and Stepanov, 2008; Nakariakov and Melnikov, 2009; Nakariakov *et al.*, 2016, and references therein). The basis of the majority of these models are magnetohydrodynamic (MHD) oscillations of coronal magnetic (current-carrying) flux tubes (loops, in particular). Typical observed periods of the HXR and microwave QPPs in solar flares are of $\sim 1-100$ s. This range of QPP periods corresponds well to the range of periods of coronal loop oscillations observed in the extreme-ultraviolet (EUV) waveband (*e.g.*, Nakariakov and Verwichte, 2005; Goddard *et al.*, 2016). This is the main argument in favor of the hypothesis that flare QPPs might be associated with MHD oscillations of coronal loops. An additional indirect argument in favor of this hypothesis is the close correlation of HXR and microwave pulsations with EUV and soft X-ray (SXR) pulsations (Dolla *et al.*, 2012; Simões *et al.*, 2013; Simões, Hudson, and Fletcher, 2015) and sunspot oscillations (Sych *et al.*, 2009) observed in some events. However, although oscillations of coronal magnetic structures (and waves in them) have been well observed for more than fifteen years, to our knowledge, no direct unambiguous and indisputable observational evidence has yet been presented that would support the link between the flare HXR QPPs and MHD oscillations and waves. We need to emphasize here that the aforementioned observational works (Simões *et al.*, 2013; Simões, Hudson, and Fletcher, 2015) concluded that it is not necessarily to explain the observed pulsations in terms of MHD oscillations or waves in coronal loops. Other mechanisms are also possible. Moreover, the pulsations observed across several wavelengths ranges by Dolla *et al.* (2012) impose strong constraints on the applicability of MHD oscillations of coronal loops as the drivers of pulsations.

Spatially resolved observations made with *Yohkoh*/HXT (Kosugi *et al.*, 1991) and RHESSI (Lin *et al.*, 2002) with a high angular resolution of up to $\approx 2.2''$ have clearly demonstrated that the HXR ($\gtrsim 30$ keV) footpoint sources are usually not stationary. Instead, they move (change their position) in the parent active regions during flares (Sakao, Kosugi, and Masuda, 1998; Fletcher and Hudson, 2002; Krucker, Hurford, and Lin, 2003; Bogachev *et al.*, 2005; Gan, Li, and Miroshnichenko, 2008; Yang *et al.*, 2009). Based on the detailed analysis of a few flares, it was shown that the sources of HXR QPPs can also move significantly during flares (Grigis and Benz, 2005; Zimovets and Struminsky, 2009; Inglis and Dennis, 2012). In the studied events the footpoint sources of the HXR QPPs moved predominantly along the magnetic polarity inversion line (MPIL) in the parent active regions of the studied flares. This indicates that the flare QPPs, at least those observed in the HXR range, are not necessarily related to MHD oscillations of coronal loops, as is commonly assumed. Instead, different pulsations are emitted successively from different magnetic flux tubes (loops) of flare arcades extended along the MPIL. This supports previous ideas about "elementary flare bursts" put forward many years ago by van Beek, de Feiter, and de Jager (1974a), de Jager and de Jonge (1978), de Jager (1979). Moreover, there is evidence (*e.g.*, Zimovets, Kuznetsov, and Struminsky, 2013) that similar scenarios can also take place in flares with microwave QPPs emitted from sources with an apparent single loop structure (Kupriyanova *et al.*, 2010). Most probably, the angular resolution of modern solar radio telescopes is insufficient to resolve thin magnetic flux tubes (loops or threads), successive triggering of which leads to the QPPs.

To our knowledge, until now, there have been no investigations of QPPs on the basis of a systematic analysis of a large number of solar flares observed in the HXR range with high

spatial resolution. All previous investigations are case studies (Grigis and Benz, 2005; Li and Gan, 2008; Zimovets and Struminsky, 2009, 2010; Inglis and Dennis, 2012; Inglis and Gilbert, 2013). Only a few of the most interesting flares accompanied by remarkable and obvious HXR QPPs were investigated in these works. It is therefore not yet possible to draw general conclusions about the physical mechanisms responsible for HXR QPPs in flares. It is still not known whether the movement of HXR sources of the QPPs is a common phenomenon or if only some specific flares are accompanied by apparent displacements of the HXR sources. It is also unclear whether the HXR sources of the QPPs manifest some special patterns (characters) of movement. The goal of our work is to investigate spatio-temporal dynamics (if present) of sources of solar HXR pulsations on the base of a systematic analysis of a large sample of flares observed with the RHESSI from the beginning of its regular operation on February 2002 until the end of June 2015 (the start of this work), *i.e.* for the fourteen-year time interval covering the decay phase of Solar Cycle 23 and the rise phase of Solar Cycle 24. This systematic approach, in contrast to case studies, can help us to understand the general picture of the sources of HXR pulsations in flares and to place some restrictions on their models.

The article is organized as follows. The method of the work is briefly explained in Section 2. The selection of solar flares for further analysis is described in Section 3. Analysis of the selected flares is presented in Section 4. The main results of the analysis of the selected flares are summarized and discussed in Section 5. Conclusions are given in Section 6.

## 2. Method

As was stated in Section 1, the main goal of this work is to perform a systematic study of the spatio-temporal evolution of sources of HXR pulsations in solar flares, using spatially resolved RHESSI observations. The first step of the work was selecting flares from the RHESSI events catalog for further detailed analysis. The flare selection procedure is described in Section 3. The idea is to select and analyze as many flares as possible that are accompanied by multiple (more than three) HXR peaks or pulsations (regardless of whether they are considered quasi-periodic) in the energy range $E_\gamma \gtrsim 50$ keV to determine some general properties of the sources of HXR pulsations.

For each event, the times of all significant HXR peaks (pulsations) above the background level in RHESSI's 50 – 100 keV (and 25 – 50 keV as well) count rates were determined and tabulated. This was necessary to decompose the analyzed flares into sequences of elementary bursts or pulsations (to the extent allowed by RHESSI's four-second time resolution). This decomposition later (Sections 4.4 – 4.7) allowed us to reconstruct images of the sources of individual HXR pulsations and to analyze the spatio-temporal evolution of these sources in the parent active regions over the course of the flares. Before these steps, we investigated some temporal properties of the identified pulsations. In particular, in Section 4.2 we analyze the time differences between successive HXR pulsations to uncover important information about the temporal structure of energy release processes in flaring regions. In Section 4.3 we also attempt to determine signatures of quasi-periodicities in the time profiles of HXR emission of the selected flares using standard techniques based on wavelet (Section 4.3.1) and Fourier (Section 4.3.2) analysis. However, we emphasize that the present work is not specifically focused on QPPs. Here we analyzed all HXR pulsations detected with RHESSI, regardless of whether they were quasi-periodic. A more focused and detailed search for quasi-periodicities in the selected flares will be presented elsewhere.

Furthermore, we reconstructed sequences of images of the sources of the identified HXR pulsations by implementing the standard reconstruction techniques on RHESSI's spatially resolved data (Section 4.4). After we synthesized cubes of the HXR images for individual pulsations in the selected flares, we superposed HXR images with the photospheric line-of-sight magnetograms (Section 4.5). After the superposition, we determined the positions of the HXR sources of all pulsations relative to the magnetic polarity inversion lines (MPILs) for each flare region. This allowed us to investigate the spatio-temporal evolution of the HXR sources from pulsation to pulsation in relation to the magnetic structure of the flare regions. Based on qualitative analysis, in Section 4.6 we attempt to categorize the selected flares (if possible) into main groups in accordance with the spatio-temporal evolution of their sources of the HXR pulsations. The last step of our investigation was the analysis of some quantitative characteristics of the spatio-temporal evolution of the sources of the pulsations relative to the MPILs. This is reported (in Section 4.7) only for one group of flares. For the other group of flares such a quantitative analysis was not possible because of the specific peculiarity of the spatio-temporal evolution of the HXR sources in these flares.

## 3. Flare Selection

We considered all events collected in the RHESSI flare catalog for the time interval from 12 February 2002 until 21 June 2015. This catalog contains around $1.1 \times 10^5$ events. The majority of these events are quite weak flares without significant fluxes of HXR emission with energies $\gtrsim 50$ keV.

For the second step, we used the RHESSI browser (http://sprg.ssl.berkeley.edu/~tohban/browser/) to manually select only those flares whose four-second light curves (time profiles) contained a series of at least four successive bursts (peaks or pulsations) in the 50 – 100 keV energy channel observed with the naked eye. It makes no sense to discuss pulsations (or QPPs) when only three or fewer peaks are presented in a flare light curve. We need to emphasize that since we studied the four-second light curves to preselect flares with multiple peaks, we may have missed some flares with short characteristic times of $\approx 8 - 12$ between neighboring peaks because these sometimes cannot be resolved with the naked eye in the quick-look images. This means that we mainly concentrated on flares with characteristic times between neighboring HXR peaks longer than $\approx 8 - 12$ s, although we show below that the studied flares were accompanied by very many such peaks (see Section 4.2).

We restricted the selection of flares to the 50 – 100 keV channel for two reasons. First, it is well known that this channel contains mainly bremsstrahlung of non-thermal (accelerated) electrons and is rarely contaminated by emission of hot thermal plasma occurring in flare regions. Sources of 50 – 100 keV HXR emission are almost always located in the chromospheric footpoints of flare loops. This allows our investigation to focus on processes directly related to particle acceleration. Second, we found 154 flares with at least four pulsations in the 50 – 100 keV RHESSI channel. This number is reasonable for analysis in comparison with the total amount of flares with pulsations observed in the less energetic 25 – 50 keV channel. On the other hand, the list of flares with pulsations in higher energy channels (*e.g.*, 100 – 300 keV) is obviously a sub-list of the flares observed in the 50 – 100 keV channel because of the inverse power-law character of HXR spectra at the energies $\gtrsim 30$ keV.

For the third step, we sifted flares from the preliminary list of 154 events that did not satisfy the following criteria:

- The flare is on the disk and no farther than 800″ from the disk center, *i.e.* its location is within $\pm 57^\circ$ of the heliographic longitudes and latitudes. This is necessary to reliably

relate the positions of the HXR sources to the magnetic field in the parent active regions (see Section 4.5).
- An impulsive phase of a flare is almost fully observed by RHESSI.
- The signal-to-noise ratio in the RHESSI 50 – 100 keV channel is sufficiently high. This is necessary to reliably identify HXR peaks in light curves and to synthesize HXR images of good quality for the analysis.
- The level of high-energy charged particles at the RHESSI detectors is low.
- The RHESSI attenuators do not change too many times during the flare impulsive phase and allow us to reconstruct images for many of the HXR peaks of a flare.

After this sifting of events, we obtained the final list of 29 flares suitable for further analysis. It should be emphasized that the criteria mentioned above are quite objective. We specifically tried to avoid subjective criteria to select flares as is often done when choosing flares with QPPs for case studies. We did not explicitly select flares with remarkable QPPs in light curves of HXR emission. All selected flares are only accompanied by at least four peaks of HXR emission in the 50 – 100 keV range, regardless of their temporal arrangement, which may be periodic, quasi-periodic, or not periodic.

Some useful general information about the selected flares is summarized in Table 1: number, date, start, peak and end times, X-ray (GOES) class, National Oceanic and Atmospheric Administration (NOAA) number and Hale class of a parent active region (AR), and the solar coordinates of a flare X-ray source given in the RHESSI catalog. As additional information we also indicated the time of the first appearance of a coronal mass ejection (CME) in the SOHO/LASCO/C2 field of view. This information was taken from the SOHO/LASCO CME Catalog (http://cdaw.gsfc.nasa.gov/CME_list/). We also note the standard types of solar decimeter/meter radio bursts that were detected during each event. We took into account only those CME and radio bursts whose appearance was within 120/30 minutes since a peak/start of a flare according to the GOES soft X-ray data.

## 4. Flare Analysis

### 4.1. Selection of Significant Peaks or Pulsations

For each selected flare we automatically identified all local minima and maxima in the four-second RHESSI background-subtracted corrected count rates in the 25 – 50 and 50 – 100 keV channels. The obtained maxima and minima correspond to local peaks and dips of the count rates. We considered only those peaks as significant whose amplitudes, that is, the highest value of the differences between a local maximum and the preceding and following minima, exceed three times the standard deviation ($3\sigma_b$) of a pre-flare background. We considered the peaks identified in this way as real peaks (pulsations) of the flare HXR emission and discarded the others as some noise fluctuations not directly related to flare processes, *e.g.*, caused by cosmic rays, radiation belt particles, astrophysical HXR and gamma-ray sources, and self-noise of the detectors.

An example of the automatic selection of significant peaks for the well-known SOL2002-11-09T13:23 flare, *i.e.* the event No. 6 according to Table 1 (*e.g.*, Grigis and Benz, 2005; Inglis and Dennis, 2012), is shown in Figure 1(a, b). The automatic routine found in total 21 peaks in the 50 – 100 keV channel for this event, and all their amplitudes are above $3\sigma_b$-level (see Figure 1(b), where the horizontal dashed line indicates the threefold standard deviation $3\sigma_b$ value of the pre-flare background). Because of this, we considered all these peaks to be significant.

**Table 1** General information about the studied events.

| 1 | 2 | 3 | 4 | 5 | 6 | 7 | 8 | 9 | 10 | 11 | 12 | 13 |
|---|---|---|---|---|---|---|---|---|---|---|---|---|
| Flare no. | Date | RHESSI flare no. | GOES start time | GOES peak time | GOES end time | GOES class | NOAA AR no. | Hale class | RHESSI flare pos. (arcsec) | Flare group no. | CME first appear. | Radio burst types |
| 1 | 14-Mar-02 | 2031402 | 01:38 | 01:50 | 02:02 | M5.7 | 9866 | $\beta\delta\gamma$ | −377, −76 | 1 | no | III, IV |
| 2 | 19-Aug-02 | 20819155 | 20:56 | 21:02 | 21:06 | M3.1 | 10069 | $\beta\delta\gamma$ | +487, −272 | 2 | no | III |
| 3 | 20-Aug-02 | 20820159 | 01:33 | 01:40 | 01:43 | M5.0 | 10069 | $\beta\delta\gamma$ | +533, −265 | 2 | 01:54 | III |
| 4 | 20-Aug-02 | 20820140 | 08:22 | 08:26 | 08:30 | M3.4 | 10069 | $\beta\delta\gamma$ | +569, −264 | 2 | 08:55 | III, V |
| 5 | 21-Aug-02 | 208211203 | 01:35 | 01:41 | 01:45 | M1.4 | 10069 | $\beta\delta\gamma$ | +693, −250 | 2 | 02:06 | II, III |
| 6 | 09-Nov-02 | 2110912 | 13:08 | 13:23 | 13:36 | M4.6 | 10180 | $\beta\delta\gamma$ | +432, −255 | 1 | 13:32 | II, III, IV |
| 7 | 29-May-03 | 30529100 | 00:51 | 01:05 | 01:12 | X1.2 | 10365 | $\beta\delta\gamma$ | +497, −106 | 1 | 01:27 | II, III, IV |
| 8 | 13-Jul-04 | 40713103 | 00:09 | 00:17 | 00:23 | M6.7 | 10646 | $\beta$ | +656, +184 | 1 | 00:54 | II, III |
| 9 | 15-Jul-04 | 4071514 | 18:15 | 18:24 | 18:28 | X1.6 | 10649 | $\beta\delta\gamma$ | −648, −233 | 2 | no | II |
| 10 | 30-Oct-04 | 4103006 | 03:23 | 03:33 | 03:37 | M3.3 | 10691 | $\beta$ | +319, +143 | 1 | 03:54 | II, III |
| 11 | 03-Nov-04 | 4110305 | 03:23 | 03:35 | 03:57 | M1.6 | 10696 | $\beta$ | −679, +101 | 1 | 03:54 | II, III, IV, V |
| 12 | 04-Nov-04 | 4110460 | 22:53 | 23:09 | 23:26 | M5.4 | 10696 | $\beta\delta$ | −283, +71 | 1 | 23:20 | III, IV |
| 13 | 06-Nov-04 | 4110630 | 00:11 | 00:34 | 00:42 | M9.3 | 10696 | $\beta\delta\gamma$ | −76, +88 | 1 | 01:32 | II, III, IV |
| 14 | 10-Nov-04 | 4111002 | 01:59 | 02:13 | 02:20 | X2.5 | 10696 | $\beta\delta\gamma$ | +710, +102 | 2 | 02:26 | II, III, IV |
| 15 | 01-Jan-05 | 5010148 | 00:01 | 00:31 | 00:39 | X1.7 | 10715 | $\beta\delta\gamma$ | −535, +125 | 1 | 00:54 | II, III, IV |
| 16 | 15-Jan-05 | 5011586 | 00:22 | 00:43 | 01:02 | X1.2 | 10720 | $\beta\delta$ | −124, +294 | 2 | no | IIIN |
| 17 | 15-Jan-05 | 50115152 | 22:25 | 23:02 | 23:31 | X2.6 | 10720 | $\beta\delta$ | +20, +310 | 1 | 23:07 | II, III, IV |
| 18 | 17-Jan-05 | 5011710 | 06:59 | 09:52 | 10:07 | X3.8 | 10720 | $\beta\delta$ | +432, +305 | 1 | 09:54 | II, III, IV |
| 19 | 19-Jan-05 | 5011911 | 08:03 | 08:22 | 08:40 | X1.3 | 10720 | $\beta\gamma$ | +696, +314 | 1 | 08:30 | II, III, IV |
| 20 | 13-May-05 | 5051310 | 16:13 | 16:57 | 17:28 | M8.0 | 10759 | $\beta$ | −174, +238 | 2 | 17:12 | II, III, IV |
| 21 | 10-Sep-05 | 5091026 | 21:30 | 22:11 | 22:43 | X2.1 | 10808 | $\beta\gamma\delta$ | −665, −254 | 2 | 21:52 | II, III, IV |
| 22 | 13-Sep-05 | 5091367 | 23:15 | 23:22 | 23:30 | X1.7 | 10808 | $\beta\gamma\delta$ | −24, −297 | 2 | 23:36 | III, IV |
| 23 | 15-Feb-11 | 11021565 | 01:44 | 01:56 | 02:06 | X2.2 | 11158 | $\beta\gamma$ | +205, −222 | 2 | 02:24 | II, III, IV, V |
| 24 | 07-Jun-11 | 11060702 | 06:16 | 06:41 | 06:59 | M2.5 | 11226 | $\beta$ | +705, −353 | 1 | 06:49 | II, III, IV |
| 25 | 06-Sep-11 | 11090678 | 22:12 | 22:20 | 22:24 | X2.1 | 11283 | $\beta\delta$ | +284, +131 | 1 | 23:06 | II, III |
| 26 | 18-Apr-14 | 14041818 | 12:31 | 13:03 | 13:20 | M7.3 | 12036 | $\beta\delta$ | +499, −229 | 2 | 13:26 | II, III, IV |
| 27 | 22-Oct-14 | 14102243 | 14:02 | 14:28 | 14:50 | X1.6 | 12192 | $\beta\delta\gamma$ | −225, −317 | 1 | 16:16 | III |
| 28 | 24-Oct-14 | 14102478 | 21:07 | 21:41 | 22:13 | X3.1 | 12192 | $\beta\delta\gamma$ | +287, −329 | 2 | 21:48 | no |
| 29 | 09-Nov-14 | 14110936 | 15:24 | 15:32 | 15:38 | M2.3 | 12205 | $\beta\gamma\delta$ | −184, +188 | 1 | no | III |

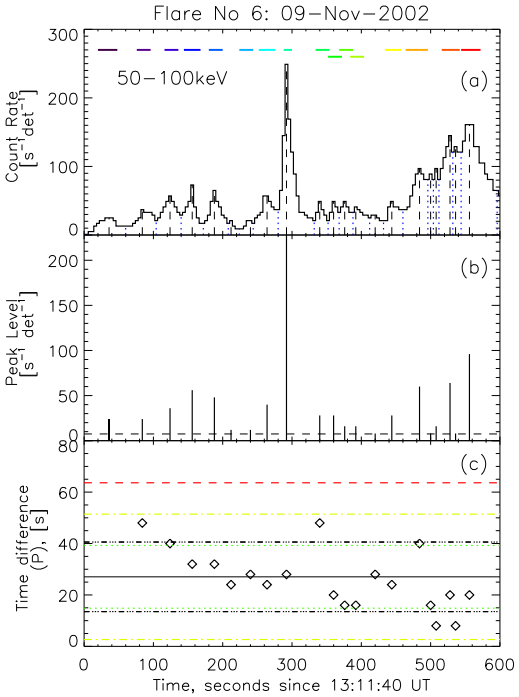


**Figure 1** Illustration of the selection of significant HXR peaks or pulsations and determination of their time differences based on the analysis of event No. 6. (a) The RHESSI background-subtracted corrected count rate in the 50 – 100 keV channel is shown by the black curve. Black dashed vertical lines indicate significant local maxima. Blue dotted vertical lines indicate all local minima. The color horizontal segments at the top mark time intervals for which HXR images were synthesized for further analysis (see Figures 5(b) and 6, as well as Figures 15, 16, 17, 18 in Appendix B). (b) Amplitudes of significant peaks are shown by black vertical lines. The horizontal dashed line indicates the threefold standard deviation ($3\sigma_b$) value of the pre-flare background. (c) Time differences ($P$) between successive significant peaks are shown by diamonds. The average value of all significant periods (*i.e.* mean time differences – $\langle P \rangle$) is shown by the black horizontal solid line. The black, green, yellow, and red horizontal dashed and dotted lines indicate levels $\langle P \rangle \pm 0.5\langle P \rangle$, $\langle P \rangle \pm 1.0\sigma_{\langle P \rangle}$, $\langle P \rangle \pm 2.0\sigma_{\langle P \rangle}$, and $\langle P \rangle \pm 3.0\sigma_{\langle P \rangle}$, respectively, where $\sigma_{\langle P \rangle}$ is the standard deviation of the time differences.

Background-subtracted corrected count rates in the RHESSI 50 – 100 keV channel with all identified significant and insignificant peaks for all selected flares (except flare No. 6) are shown in the top panels of Figures 11, 12, 13, 14 in Appendix A. The total numbers of significant peaks ($n_p$) in the 25 – 50 and 50 – 100 keV channels are shown in columns 2 and 7 of Table 2, respectively.

We need to note that for the sake of convenience we did not use the original RHESSI count rates but rather the corrected count rates. We found that the use of the corrected count rates did not significantly (within 10 %) influence the results of our specific analysis in comparison with the use of the uncorrected count rates, especially in the 50 – 100 keV band, which is of the principal importance for this work.

### 4.2. Time Differences Between Pulsations

Knowing the times of significant peaks for each event, we calculated time differences ($P$) between successive peaks (see bottom panels of Figure 1 and Figures 11 – 14 in Ap-

**Table 2** Results of the analysis of the RHESSI background-subtracted corrected count rates in the 25 – 50 and 50 – 100 keV channels.

| 1 | 2 | 3 | 4 | 5 | 6 | 7 | 8 | 9 | 10 | 11 | 12 | 13 | 14 | 15 |
|---|---|---|---|---|---|---|---|---|---|---|---|---|---|---|
| Flare no. | $n_p$ | $\langle P\rangle$ [s] | $\sigma_P$ [s] | $N$ of peaks in $\langle P\rangle \pm 0.5\langle P\rangle$ | $N$ of peaks in $\langle P\rangle \pm 3.0\sigma_P$ | $n_p$ | $\langle P\rangle$ [s] | $\sigma_P$ [s] | $N$ of peaks in $\langle P\rangle \pm 0.5\langle P\rangle$ | $N$ of peaks in $\langle P\rangle \pm 3.0\sigma_P$ | $k_p$ | $\langle P'\rangle$ [s] | $\sigma(P')$ [s] | $r_p$ |
| | 25 – 50 keV channel | | | | | 50 – 100 keV channel | | | | | 50 – 100 keV channel | | | |
| 1 | 27 | 22 | 13 | 19 (70 %) | 26 (96 %) | 25 | 28 | 25 | 10 (40 %) | 24 (96 %) | 10 | 61 | 35 | 2.5 |
| 2 | 5 | 19 | 12 | 2 (40 %) | 5 (100 %) | 5 | 23 | 10 | 3 (60 %) | 5 (100 %) | 5 | 23 | 10 | 1.0 |
| 3 | 15 | 20 | 11 | 8 (53 %) | 15 (100 %) | 9 | 26 | 18 | 5 (56 %) | 9 (100 %) | 7 | 25 | 13 | 1.3 |
| 4 | 9 | 21 | 12 | 6 (67 %) | 9 (100 %) | 9 | 17 | 6 | 7 (78 %) | 9 (100 %) | 5 | 22 | 4 | 1.8 |
| 5 | 10 | 21 | 7 | 8 (80 %) | 10 (100 %) | 9 | 26 | 21 | 6 (67 %) | 9 (100 %) | 5 | 18 | 4 | 1.8 |
| 6 | 21 | 27 | 13 | 16 (76 %) | 21 (100 %) | 21 | 26 | 12 | 14 (67 %) | 21 (100 %) | 16 | 36 | 13 | 1.3 |
| 7 | 18 | 28 | 15 | 7 (39 %) | 18 (100 %) | 13 | 31 | 17 | 7 (54 %) | 13 (100 %) | 6 | 70 | 7 | 2.2 |
| 8 | 15 | 16 | 5 | 13 (87 %) | 15 (100 %) | 13 | 19 | 5 | 13 (100 %) | 13 (100 %) | 11 | 21 | 11 | 1.2 |
| 9 | 7 | 17 | 7 | 7 (100 %) | 7 (100 %) | 7 | 20 | 7 | 7 (100 %) | 7 (100 %) | 5 | 23 | 2 | 1.4 |
| 10 | 14 | 22 | 12 | 8 (57 %) | 14 (100 %) | 13 | 22 | 11 | 8 (62 %) | 13 (100 %) | 8 | 34 | 13 | 1.6 |
| 11 | 15 | 19 | 7 | 13 (87 %) | 15 (100 %) | 12 | 20 | 9 | 8 (67 %) | 12 (100 %) | 6 | 30 | 12 | 2.0 |
| 12 | 36 | 24 | 26 | 19 (53 %) | 36 (100 %) | 19 | 40 | 31 | 12 (63 %) | 18 (95 %) | 8 | 46 | 28 | 2.4 |
| 13 | 6 | 43 | 23 | 3 (50 %) | 6 (100 %) | 9 | 30 | 22 | 6 (67 %) | 9 (100 %) | 7 | 39 | 22 | 1.3 |
| 14 | 31 | 19 | 10 | 17 (55 %) | 31 (100 %) | 13 | 44 | 22 | 10 (77 %) | 12 (92 %) | 8 | 47 | 10 | 1.6 |
| 15 | 12 | 22 | 14 | 9 (75 %) | 12 (100 %) | 7 | 19 | 9 | 3 (43 %) | 7 (100 %) | 5 | 22 | 10 | 1.4 |
| 16 | 10 | 19 | 11 | 5 (50 %) | 10 (100 %) | 9 | 23 | 12 | 9 (56 %) | 9 (100 %) | 8 | 30 | 6 | 1.1 |
| 17 | 54 | 39 | 44 | 27 (50 %) | 54 (100 %) | 103 | 22 | 19 | 87 (84 %) | 100 (97 %) | 15 | 86 | 25 | 6.9 |
| 18 | 36 | 22 | 15 | 27 (75 %) | 35 (97 %) | 32 | 25 | 18 | 18 (56 %) | 32 (100 %) | 13 | 55 | 37 | 2.5 |
| 19 | 55 | 20 | 15 | 46 (84 %) | 54 (98 %) | 18 | 60 | 46 | 8 (44 %) | 18 (100 %) | 11 | 87 | 47 | 1.6 |
| 20 | 20 | 21 | 9 | 16 (80 %) | 20 (100 %) | 14 | 33 | 34 | 6 (43 %) | 14 (100 %) | 6 | 86 | 25 | 2.3 |
| 21 | 103 | 23 | 25 | 65 (63 %) | 102 (99 %) | 89 | 31 | 34 | 44 (49 %) | 87 (98 %) | 12 | 133 | 30 | 7.4 |
| 22 | 6 | 27 | 30 | 1 (17 %) | 6 (100 %) | 13 | 33 | 34 | 6 (46 %) | 13 (100 %) | 6 | 22 | 12 | 2.2 |
| 23 | 35 | 16 | 7 | 31 (89 %) | 35 (100 %) | 29 | 20 | 9 | 20 (69 %) | 29 (100 %) | 12 | 33 | 7 | 2.4 |
| 24 | 36 | 26 | 14 | 21 (58 %) | 36 (100 %) | 41 | 23 | 14 | 29 (71 %) | 40 (98 %) | 13 | 51 | 11 | 3.2 |
| 25 | 20 | 21 | 14 | 13 (65 %) | 20 (100 %) | 10 | 28 | 21 | 3 (33 %) | 10 (100 %) | 8 | 23 | 8 | 1.3 |
| 26 | 23 | 24 | 16 | 15 (65 %) | 23 (100 %) | 30 | 20 | 13 | 18 (60 %) | 29 (97 %) | 11 | 48 | 35 | 2.7 |
| 27 | 10 | 21 | 10 | 5 (50 %) | 10 (100 %) | 6 | 35 | 10 | 6 (100 %) | 6 (100 %) | 5 | 30 | 6 | 1.2 |
| 28 | 34 | 17 | 8 | 22 (65 %) | 34 (100 %) | 15 | 27 | 18 | 11 (73 %) | 15 (100 %) | 9 | 44 | 17 | 1.7 |
| 29 | 8 | 20 | 12 | 4 (50 %) | 8 (100 %) | 7 | 19 | 5 | 7 (100 %) | 7 (100 %) | 7 | 26 | 8 | 1.0 |

pendix A). The total number of time differences in a flare is $N_P = n_p - 1$. The average value of all time differences of a particular flare was calculated and called formally the mean time difference of this flare ($\langle P \rangle$; see columns 3 and 8 in Table 2). For each flare we also calculated standard deviations of time differences ($\sigma_P$; see columns 4 and 9 in Table 2). This value can be considered as a measure of the spread of time differences from the average value, *i.e.* from the mean time difference $\langle P \rangle$. Intuitively, when the spread is not broad, we might speculate whether these are QPPs. However, as we mentioned in Section 1, there is no strict definition of QPPs, and it is not clear what to consider a broad or narrow spread around the average value. We therefore calculated for each flare several different levels relative to its own mean time difference: $\langle P \rangle \pm 0.5\langle P \rangle$, $\langle P \rangle \pm 1.0\sigma_P$, $\langle P \rangle \pm 2.0\sigma_P$, and $\langle P \rangle \pm 3.0\sigma_P$. They are shown by different horizontal lines in the bottom panels of Figure 1 and Figures 11 – 14 in Appendix A. Numbers (percentages) of significant peaks within the $\langle P \rangle \pm 0.5\langle P \rangle$ and $\langle P \rangle \pm 3.0\sigma_P$ ranges for all selected flares in the 25 – 50 and 50 – 100 keV channels are presented in columns 5 – 6 and 10 – 11 of Table 2, respectively.

In the majority of flares (except for seven events: Nos. 1, 12, 14, 17, 21, 24, and 26) all time differences in the 50 – 100 keV channel are within the $\langle P \rangle \pm 3.0\sigma_P$ range (the same is true for the 25 – 50 keV channel). This indicates indirectly that $P$ is a random value, which may be distributed normally around some average value (not necessary $\langle P \rangle$). We tried to check this by plotting the time difference distributions in the form of histograms. However, the number of significant pulsations is smaller than 16 in 19 out of 29 studied flares. It does not make sense to build distributions on such a small number of data points.

Nonetheless, 10 flares (Nos. 1, 6, 12, 17, 18, 19, 21, 23, 24, and 26) have more than 16 pulsations each. For these flares we plot the time difference distributions in Figure 2. The distributions of seven of these flares (Nos. 1, 17, 18, 19, 21, 24, and 26) have sharply decreasing shapes with maxima around $P \approx 8 - 20$ s, *i.e.* around the lower threshold of time differences ($P_{\rm thr} = 8$ s) that can be, in principle, identified in data sets with four-second cadence. This indicates that in the majority of the studied flares RHESSI does not allow us to resolve the temporal fine-structure of the HXR emission and that the maxima of the real time difference distributions, if they exist, are somewhere below $P_{\rm thr} = 8$ s.

However, in 3 of these 10 flares (Nos. 6, 12, and 23) the time difference distribution has a bell-like shape (although not ideal, in particular, because of poor statistics) with maxima in the range of $P \approx 20 - 40$ s. The positions of these maxima coincide well with mean time differences $\langle P \rangle$ and the widths of these distributions at half of their maxima are close to the standard deviations of time differences in these flares. This indicates that time differences between successive HXR pulsations in these events are random variables distributed normally around their average values, $\langle P \rangle$, and that the four-second RHESSI cadence can be enough to resolve temporal variations of HXR emission in these particular flares.

We also plot the collective time difference distributions combined for all 29 studied flares (see Figure 3) to explore the general picture. The picture is as expected: the distributions have exponentially decreasing shapes with maxima around $P \approx 8 - 30$ s, *i.e.* around the lower threshold of the time differences ($P_{\rm thr} = 8$ s) that is possible for the data with four-second cadence. The best-fit exponential functions $f = a \exp(-P/b)$ have the following coefficients for the 50 – 100 keV and 25 – 50 keV channels: $a_{50} = 1013.09 \pm 7.57$ and $b_{50} = 17.78 \pm 0.11$ s, and $a_{25} = 1979.97 \pm 14.18$ and $b_{25} = 15.62 \pm 0.08$ s, respectively.

### 4.3. Search for Quasi-periodicities in Flare Light Curves

To search for possible quasi-periodicities in the light curves of the HXR emission of the studied flares, we used standard spectral analysis methods. We would like to emphasize, once again, that this is not the main goal of this work. We applied these standard methods

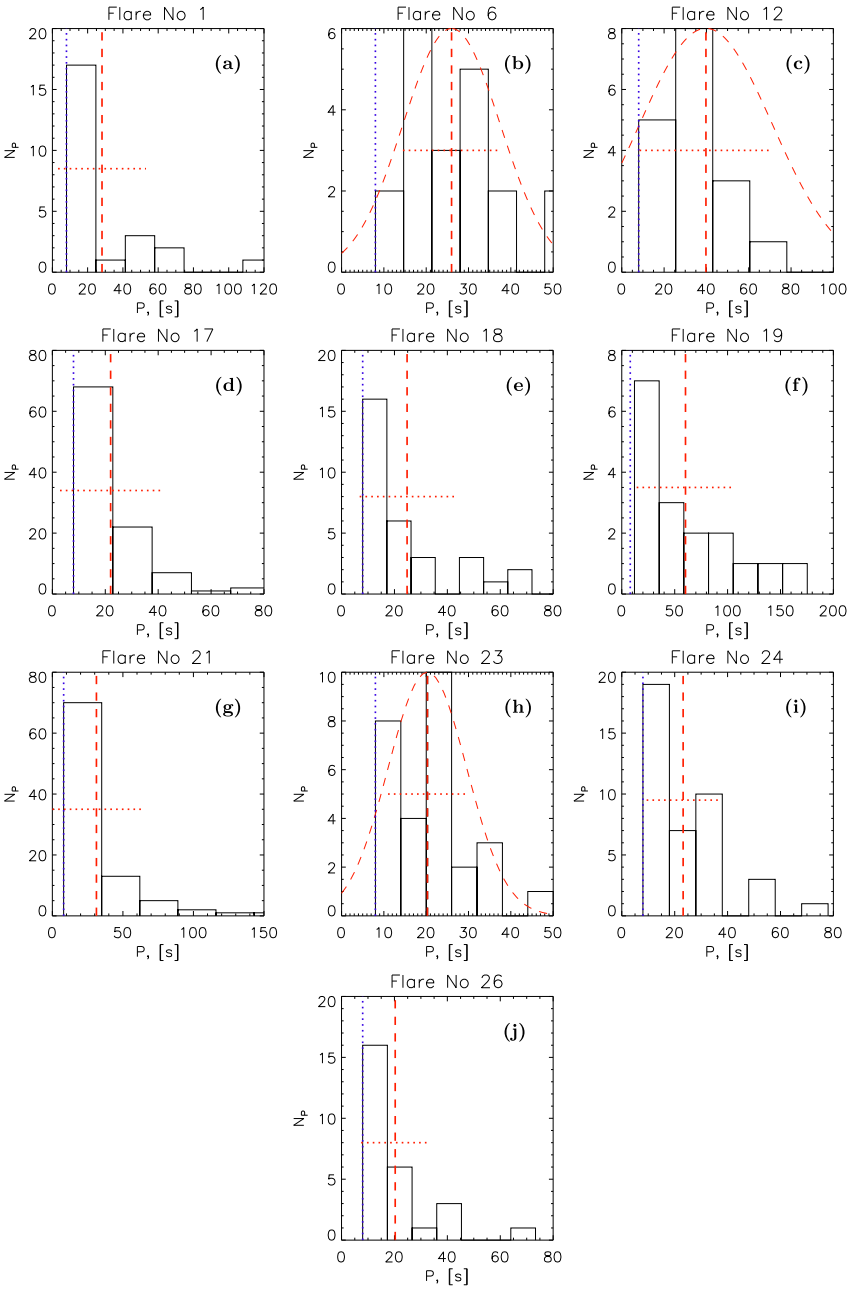


**Figure 2** Distributions of time differences ($P$) found in the four-second RHESSI background-subtracted corrected count rates in the 50 – 100 keV channel for flares No. 1, 6, 12, 17, 18, 19, 21, 23, 24, and 26 (see Table 1). The red vertical dashed line shows the mean time difference $\langle P \rangle$ of a given flare. The red horizontal dotted line shows the standard deviation ($\sigma_P$) of the time differences at half the maximum level. The blue vertical dotted line shows the lower threshold ($P_{\rm thr} = 8$ s) of the time differences, which can be found in the four-second count rates. The red thin dashed curves in panels (b), (c), and (h) show Gaussian functions with corresponding $\langle P \rangle$ and $\sigma_P$ parameters for flares No. 6, 12, and 23, respectively, whose distributions are similar to a bell-like shape.

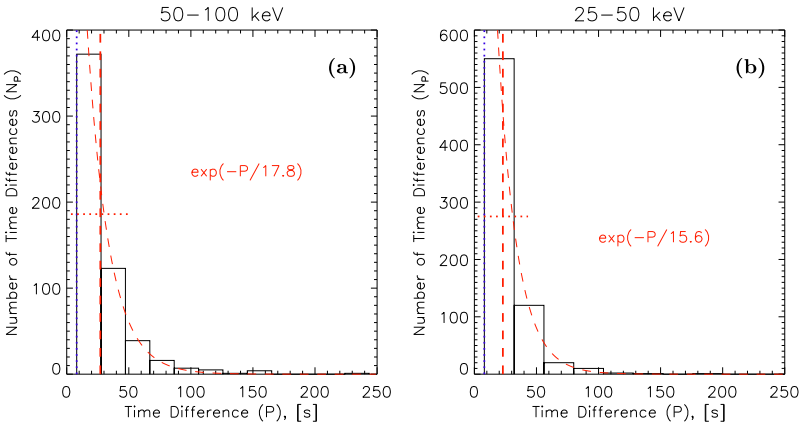


**Figure 3** Combined distributions of the time differences ($P$) found in the four-second RHESSI background–subtracted corrected count rates in the 50 – 100 keV (a) and 25 – 50 keV (b) channels for all 29 studied flares. The red vertical dashed line shows the averaged time difference. The red horizontal dotted line shows the standard deviation of time differences at half the maxima of the distributions. The blue vertical dotted line shows the lower threshold ($P_{\rm thr} = 8$ s) of time differences, which can be found in the four-second count rates. The red thin dashed curves show Gaussian functions found by the best fit of the distributions.

to make our analysis more comprehensive, since these methods are often used by various authors when analyzing pulsations of flare emissions.

First (Section 4.3.1), we used the wavelet analysis procedure by Torrence and Compo (1998) to obtain the wavelet power spectra and derive frequency–temporal structures of the investigated signals. Second (Section 4.3.2), we used the Fast Fourier Transform (the "*FFT.pro*" function within IDL) to calculate the normalized periodograms to search for significant spectral peaks in the signals. We used the pre-flare background-subtracted RHESSI-corrected count rates, normalized to their maxima, without any detrending. This approach ensures that we analyzed the original flare signal without introducing any significant distortions due to empirical detrending, which could affect the results of a spectral analysis (see, *e.g.*, Vaughan, 2005; Gruber *et al.*, 2011). To take into account the red-noise influence, we searched spectral peaks above the red-noise level at significance levels of 95.0 % and 99.7 %.

### *4.3.1. Wavelet Analysis*

The results of the wavelet analysis for the representative event No. 6 are shown in Figure 4(a – c). The characteristic timescale of HXR QPPs at a significance level of 95.0 % varies from 25 s to 40 s. However, no QPPs are detected at a significance level of 99.7 % for this event.

The results of the wavelet analysis for all studied events are summarized in Table 3 at significance levels of 95.0 % and 99.7 % (columns 4 and 5, respectively). Quasi-periodicities of HXR pulsations have been found in five events at a significance level of 95.0 %. Only three of these events have periodicities at a significance level of 99.7 %.

### *4.3.2. Periodogram Analysis*

The normalized frequency spectrum for event No. 6 is shown in Figure 4(d). It is clearly seen that there are no spectral peaks at significance levels of 95.0 % and 99.7 % in this event.

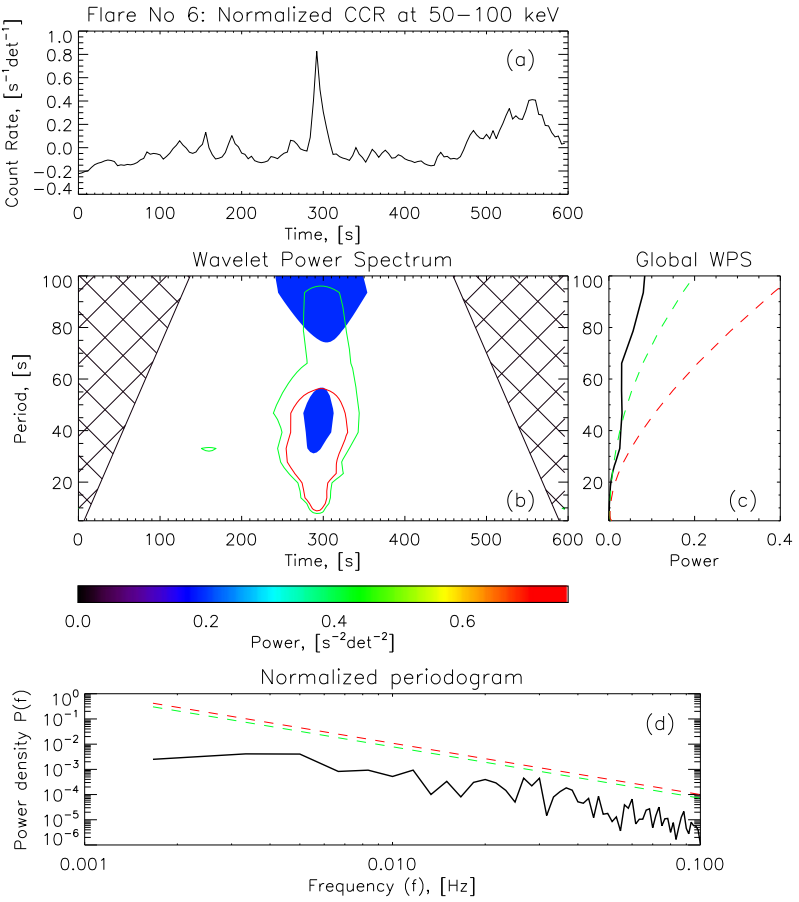


**Figure 4** The results of the wavelet and periodogram analysis for event No. 6. (a) RHESSI background–subtracted corrected count rate in the 50 – 100 keV channel normalized to its maximum. (b) Wavelet power spectrum with significance levels of 95.0 % (green contour) and 99.7 % (red contour) above the red noise. The cross-hatched region is the cone of influence, above which everything is dubious. (c) Global wavelet power spectrum. The colored lines indicate significance levels of 95.0 % (dashed green line) and 99.7 % (dashed red line) above the red noise. (d) Normalized periodogram with significance levels above the red noise of 95.0 % (dashed green line) and 99.7 % (dashed red line).

The spectral peaks (periods) of the HXR pulsations for all selected events using FFT are shown in Table 3. Four events have quasi-periodicities at a significance level of 95.0 %. Only two of these events have quasi-periodicities at a significance level of 99.7 %. These periods correspond to near-the-edge frequencies of the calculated spectra. Moreover, these two events differ from those three events for which quasi-periodicities were found using the wavelet analysis. This is reason to seriously doubt the real significance of quasi-periodicities we found.

When we combine the results of the wavelet and periodogram analysis, we can conclude that quasi-periodicities in solar flare HXR emission are, probably, quite a rare phenomenon when the red-noise character of the signals is taken into account. This is an expected result (see Gruber *et al.*, 2011; Inglis, Ireland, and Dominique, 2015).

**Table 3** Results of the search for quasi-periodicities of HXR emission in the studied flares. The characteristic timescales found in the RHESSI background-subtracted, normalized-to-maximum, corrected count rates in the 50 – 100 keV channel are shown above the red-noise level for significance levels of 95.0 % and 99.7 %.

| 1 | 2 | 3 | 4 | 5 | 6 | 7 |
|---|---|---|---|---|---|---|
| Flare no. | Start time UT | End time UT | Periods from wavelet analysis [s] | | Periods from periodogram analysis [s] | |
| | | | 95.0 % | 99.7 % | 95.0 % | 99.7 % |
| 1 | 01:41:00 | 01:53:00 | no | no | 8.1 – 9.1 | 8.6 |
| 2 | 21:00:00 | 21:02:00 | no | no | no | no |
| 3 | 01:38:00 | 01:43:00 | no | no | no | no |
| 4 | 08:24:00 | 08:27:00 | no | no | no | no |
| 5 | 01:38:00 | 01:43:00 | 26 – 28 | no | no | no |
| 6 | 13:11:40 | 13:21:40 | 25 – 40 | no | no | no |
| 7 | 01:00:00 | 01:08:00 | no | no | no | no |
| 8 | 00:13:00 | 00:18:00 | no | no | no | no |
| 9 | 18:21:30 | 18:24:00 | no | no | no | no |
| 10 | 03:29:00 | 03:35:00 | no | no | no | no |
| 11 | 03:28:00 | 03:33:00 | no | no | no | no |
| 12 | 22:53:00 | 23:08:00 | 40 – 148 | 50 – 130 | no | no |
| 13 | 00:28:00 | 00:33:00 | no | no | no | no |
| 14 | 02:05:00 | 02:15:00 | no | no | no | no |
| 15 | 00:27:00 | 00:32:00 | no | no | no | no |
| 16 | 00:39:00 | 00:43:00 | no | no | no | no |
| 17 | 22:30:00 | 23:10:00 | no | no | 400 – 800 | 400 |
| 18 | 09:41:00 | 09:55:00 | 50 – 130 | 80 – 110 | no | no |
| 19 | 08:11:00 | 08:31:00 | 90 – 290 | 90 – 235 | no | no |
| 20 | 16:37:00 | 16:45:00 | no | no | no | no |
| 21 | 21:30:00 | 22:20:00 | no | no | 8.2 | no |
| 22 | 23:18:00 | 23:22:00 | no | no | no | no |
| 23 | 01:48:00 | 01:58:00 | no | no | no | no |
| 24 | 06:25:00 | 06:41:00 | no | no | no | no |
| 25 | 22:12:00 | 22:24:00 | no | no | no | no |
| 26 | 12:50:00 | 13:00:00 | no | no | no | no |
| 27 | 14:05:00 | 14:09:00 | no | no | 8.6 | no |
| 28 | 21:09:00 | 21:19:00 | no | no | no | no |
| 29 | 15:28:00 | 15:31:00 | no | no | no | no |

### 4.4. HXR Image Reconstruction

After we identified significant peaks in the RHESSI 50 – 100 keV (and 25 – 50 keV) corrected count rates for all selected flares, we reconstructed (synthesized) images for some of them using RHESSI data. We used the CLEAN and PIXON algorithms (Hurford *et al.*, 2002) within the standard RHESSI Solar SoftWare (SSW) package (http://www.lmsal.com/solarsoft/). The CLEAN algorithm was used for the preliminary analysis of flare regions and the PIXON algorithm for detailed analysis of spatio-temporal evolution of the HXR sources

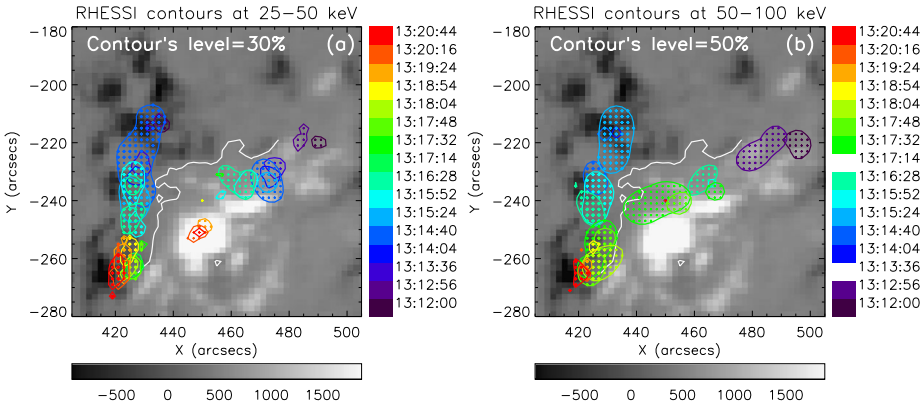


**Figure 5** Comparison of the positions of HXR sources in the 25 – 50 keV (a) and 50 – 100 keV (b) energy ranges for significant HXR peaks of flare No. 6 (see Figure 1). The PIXON algorithm was used to reconstruct the HXR sources shown. The background image is the photospheric line-of-sight magnetogram obtained with SOHO/MDI. The magnetic field color bar (in gauss) is presented below the images. The MPIL is shown by the white curves. The colors of the HXR sources correspond to the times of the HXR peaks shown near the color bars to the right of the images. White in the color bar (right) indicates that there are no good HXR images for these peaks. The contour levels of the HXR sources (in percentage of the maximum brightness) are labeled in the figure.

of pulsations. We usually used detectors 2 – 8 with the CLEAN algorithm and all detectors 1 – 9 with PIXON. The size of the reconstructed images is 64 × 64 pixels with an angular pixel size of 1″ or 2″, depending on the size of the flare region observed in the HXR range.

To synthesize images we selected time intervals of 12 to 40 s duration around the maxima of significant peaks. For some peaks we were unable to synthesize images because the attenuators changed. However, the main problem was the low signal-to-noise ratio. This was especially pronounced in the 50 – 100 keV range, in the 25 – 50 keV range the situation was better in general. Unfortunately, we were unable to synthesize images of reliable quality for some short-duration significant peaks (≈ 8 – 12 s), especially in the 50 – 100 keV range. We therefore restricted our work by reconstructing images mainly in the 25 – 50 keV range. The effective area of the RHESSI detectors, even in the 25 – 50 keV range, is not enough to reconstruct images of reliable quality for some low-amplitude short-duration peaks. In some cases, we needed to synthesize images over time intervals containing several peaks (from 2 to 4) to increase the signal-to-noise ratio. All time intervals selected for image reconstruction are marked by colored horizontal segments in the top panels of Figure 1 and Figures 11 – 14 in Appendix A. The colors of these segments correspond to the colors of the contours used to show the HXR sources in Figures 5 – 6 and Figures 15 – 18 in Appendix B.

It is known (*e.g.*, Veronig and Brown, 2004) that in some flares, HXRs in the 25 – 50 keV range are emitted from coronal thick-target sources. However, our experience shows that this situation is rare, and in the majority of cases, HXR emission in the 25 – 50 keV range is predominantly bremsstrahlung of non-thermal electrons emitted mainly from the chromospheric (or low coronal) footpoints of flare loops. As an example, Figure 5 shows the positions of HXR sources in the 25 – 50 keV (a) and 50 – 100 keV (b) energy ranges for the significant peaks found in flare No. 6. The spatio-temporal evolution of HXR sources for those peaks for which it was possible to synthesize images of reliable quality are in general similar for both energy ranges. The difference is only in some minor details. This is typical for the majority of the analyzed flares.

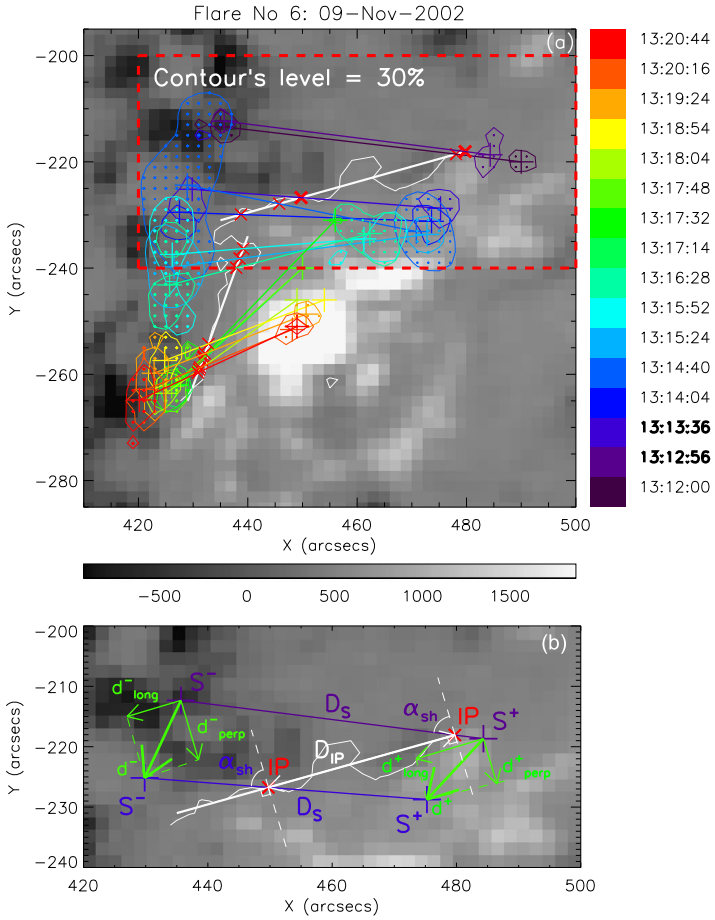


**Figure 6** (a) Spatio-temporal evolution of the sources of the HXR pulsations in flare No. 6 of group 1. The number and date of the flare are shown above. The PIXON algorithm was used to reconstruct the HXR sources shown. The background image is the photospheric line-of-sight magnetogram obtained with the SOHO/MDI. The magnetic field color bar (in gauss) is presented below. The colors of the HXR sources correspond to the times of the HXR peaks shown near the color bar to the right. The contour level of the HXR sources is labeled in the image. Large color crosses show the average positions (centroids) of the HXR sources at the corresponding times. The linear sizes of these crosses are equal to twice the FWHM of the RHESSI collimator number 1. Straight color lines connect paired HXR sources located in opposite magnetic polarities. Small red crosses indicate intersection points (IPs) of these lines with the approximate MPIL (thick white lines). The real MPIL derived from the magnetogram is shown by the thin white curve. (b) Zoom of the parent active region within the red dashed boundaries indicated in panel (a) with notations of the quantitative characteristics of the HXR sources dynamics calculated in Section 4.7. Paired HXR sources $S^+$ and $S^-$ in positive and negative magnetic polarities for the two successive significant HXR peaks are shown by different colors. The corresponding times of these peaks are marked in bold font near the color bar to the right of the panel (a). The thick green arrows $d^+$ and $d^-$ indicate the total displacements of sources $S^+$ and $S^-$ between two successive HXR peaks. The white dashed lines are the perpendiculars to the approximate MPIL at the intersection points (IPs).

We found that only five flares from our list (Nos. 3, 9, 16, 21, and 28) manifest signatures of coronal emission in the 25 – 50 keV channel; in some individual peaks the 25 – 50 keV sources were situated above the magnetic polarity inversion lines (MPIL; see Section 4.5)

and/or had a loop-like shape. However, this did not strongly complicate our analysis of the spatio-temporal dynamics of the HXR sources and did not strongly influence the main results.

### 4.5. HXR Source Location

Since the magnetic field plays a crucial role in solar flares and because accelerated electrons are magnetized, it is of principal importance to investigate spatio-temporal evolution of flare HXR sources with respect to the magnetic field of the parent active regions. For this purpose, we used the photospheric line-of-sight magnetograms obtained with the SOHO/MDI (Scherrer *et al.*, 1995) and SDO/HMI (Scherrer *et al.*, 2012) instruments in 2002 – 2010 and 2011 – 2015, respectively. For each flare we selected a magnetogram that was closest in time to the beginning of a flare impulsive phase. Using the "*drot_map.pro*" routine within SSW, we rotated the magnetograms to an epoch in the middle of the impulsive phase of the corresponding flares. For each magnetogram we found MPILs as curves separating positive and negative magnetic polarities in a flare region. An MPIL is a natural object, always present in active regions, relative to which it makes sense to investigate dynamics of flare HXR sources (*e.g.*, Bogachev *et al.*, 2005; Grigis and Benz, 2005; Gan, Li, and Miroshnichenko, 2008; Zimovets and Struminsky, 2009).

For each significant HXR peak for which it was possible to synthesize RHESSI images of good quality, we found solar coordinates of all pixels within 15 %, 20 %, 30 %, or 40 % levels from the brightest pixel at a given image. The percentage level was fixed for all peaks of the same flare (*e.g.* 30 % or 40 %), but it varied from flare to flare. The selection of levels is quite subjective. We tried to choose levels so that for each image there was at least one HXR contour on either side of an MPIL. For the majority of flares we chose the 30 % level.

We automatically separated pixels located in different magnetic polarities. For each image we separately determined the average solar coordinates of all pixels located in positive and negative polarities. These coordinates were used further to obtain quantitative characteristics of the dynamics of HXR sources (see Section 4.7). HXR sources located in positive and negative magnetic polarities were denoted as $S^+$ and $S^-$, respectively. For each flare, the $S^+$ and $S^-$ sources were overplotted on a magnetogram by different colors for different peaks. This allowed us to clearly visualize the spatio-temporal evolution (if present) of HXR sources from peak to peak relative to the MPILs in the parent active regions.

### 4.6. Separation of Flares into Two Groups

After visually inspecting the maps of the spatio-temporal evolution of the HXR sources from peak to peak and of the morphology of the parent active regions of all flares we studied, we found that all events can be subdivided into (at least) two groups.

Group 1 (16 flares, *i.e.* 55 % of all flares) consists mainly of two-ribbon flares with systematic dynamics of the HXR sources relative to the MPILs, which had simple elongated shapes in these flare regions. For many of the significant HXR peaks in these flares it was possible to identify paired HXR sources ($S^+$ and $S^-$) located in regions of different magnetic polarities. Most probably, these paired HXR sources are situated in opposite footpoints of the flare magnetic flux tubes (loops). By systematic dynamics we mean that the paired HXR sources show one of the four basic types of motions or their combinations (*e.g.*, Bogachev *et al.*, 2005; Ji *et al.*, 2006; Gan, Li, and Miroshnichenko, 2008; Yang *et al.*, 2009):

(Type A) $S^+$ and $S^-$ move in the same direction parallel to an MPIL;
(Type B) $S^+$ and $S^-$ move in opposite directions parallel to an MPIL;
(Type C) $S^+$ and $S^-$ move away from and perpendicular to an MPIL;
(Type D) $S^+$ and $S^-$ move toward and perpendicular to an MPIL.

In group 2 (13 events, *i.e.* 45 % of all flares) the HXR sources appeared and moved more chaotically than in the group 1 events. It was difficult to unambiguously identify paired HXR sources and to determine their type of movement in these cases. In the majority of group 2 flare regions several separated MPILs of complicated shape were present simultaneously.

The group classification of each analyzed flare is shown in column 11 of Table 1. Types of paired HXR source motions identified in the group 1 flares are shown in column 16 of Table 4. Maps of the spatio-temporal evolution of the HXR sources for all studied events are shown in Figures 15 – 18 in Appendix B.

The mean time differences averaged over group 1 and group 2 flares and their standard deviations are: $\langle P^{g1} \rangle \approx 27.9$ s, $\sigma_P^{g1} \approx 10.5$ s and $\langle P^{g2} \rangle \approx 26.4$ s, $\sigma_P^{g2} \approx 7.1$ s, respectively, *i.e.* they are almost the same. The mean number of significant peaks found in group 1 and group 2 flares and their standard deviations are also almost the same: $n_{\rm p}^{g1} \approx 21.8$, $\sigma_{\rm p}^{g1} \approx 23.7$ and $n_{\rm p}^{g2} \approx 19.3$, $\sigma_{\rm p}^{g2} \approx 22.3$, respectively. Thus, the temporal characteristics of both groups of flares are very similar to each other. This indicates that the separation of flares into two groups is rather arbitrary and subjective and, possibly, has no deep physical meaning. We discuss this in Section 5. Nonetheless, for group 1 flares it is possible to quantitatively estimate some important physical characteristics of the dynamics of paired sources of HXR pulsations (see Section 4.7), which is hard to do for group 2 flares.

### 4.7. Quantitative Characterization of the Dynamics of the HXR Sources

As was mentioned in Section 4.5, it is possible to estimate some useful quantitative characteristics of the spatio-temporal evolution of paired $S^+$ and $S^-$ sources of the HXR pulsations in group 1 flares. For the selected peaks of each group 1 flare for which it was possible to reconstruct images of good quality, we calculated the following characteristics (see Figure 6(b) for their visual explanation):

- The distance ($D_{\rm S}$) between paired $S^+$ and $S^-$ sources, which gives an estimate of the length of a flaring loop (using a coefficient, *e.g.*, $\pi/2$, when a loop has a semi-circular shape) at a given HXR peak.
- The shear angle ($\alpha_{\rm sh}$) between an MPIL and a segment connecting $S^+$ and $S^-$ sources. This angle provides an estimation of the shear angle of a flaring loop and, to some extent, information about the deviation of the magnetic field of a loop from the potential state, which is a measure of its free magnetic energy.
- The coordinates of an intersection point (IP) between a line segment connecting $S^+$ and $S^-$ sources and an MPIL.
- The distance ($D_{\rm IP}$) between IPs at two successive HXR peaks. This distance provides an estimate of the spacing (in the image plane) between two flaring loops (two bundles of loops) from which two successive HXR peaks were emitted.
- The velocity ($v_{\rm IP}$) of the apparent IP displacement between two successive HXR peaks. It is calculated as the ratio between $D_{\rm IP}$ and a time difference between two corresponding peaks. This velocity provides an estimate of the velocity of possible triggers of the energy release along an MPIL direction.
- The parallel ($v_\parallel^+$ and $v_\parallel^-$), perpendicular ($v_\perp^+$ and $v_\perp^-$), and total ($v^+$ and $v^-$) velocities of the apparent displacement of $S^+$ and $S^-$ sources relative to an MPIL.

**Table 4** Results of the analysis of the quantitative characteristics of the source dynamics of HXR pulsations in group 1 flares.

| 1 | 2 | 3 | 4 | 5 | 6 | 7 | 8 | 9 | 10 | 11 | 12 | 13 | 14 | 15 | 16 |
|---|---|---|---|---|---|---|---|---|---|---|---|---|---|---|---|
| Flare no. | $\langle D_S \rangle$ [Mm] | $\sigma(D_S)$ [Mm] | $\langle \alpha_{sh} \rangle$ [Deg] | $\sigma(\alpha_{sh})$ [Deg] | $\langle D_{IP} \rangle$ [km] | $\sigma(D_{IP})$ [km] | $\langle v_{IP} \rangle$ [km s$^{-1}$] | $\sigma(v_{IP})$ [km s$^{-1}$] | $\langle v^+ \rangle$ [km s$^{-1}$] | $\sigma(v^+)$ [km s$^{-1}$] | $\langle v^- \rangle$ [km s$^{-1}$] | $\sigma(v^-)$ [km s$^{-1}$] | $R^+$ | $R^-$ | Types of dynamics |
| 1 | 24 | 8 | 40 | 17 | 1600 | 1460 | 36 | 36 | 57 | 61 | 57 | 63 | 2.4 | 0.6 | A + D + C |
| 6 | 29 | 6 | 53 | 16 | 4767 | 6236 | 128 | 154 | 160 | 156 | 105 | 93 | 1.8 | 3.8 | A + D |
| 7 | 16 | 4 | 32 | 15 | 965 | 860 | 14 | 12 | 56 | 93 | 90 | 66 | 1.3 | 1.8 | A + C |
| 8 | 10 | 4 | 28 | 18 | 2932 | 7876 | 120 | 301 | 71 | 52 | 61 | 91 | 1.3 | 1.1 | A + B + C |
| 10 | 13 | 4 | 48 | 16 | 1612 | 1440 | 51 | 50 | 53 | 48 | 37 | 49 | 1.4 | 2.1 | A |
| 11 | 22 | 4 | 40 | 6 | 1570 | 1485 | 61 | 51 | 110 | 87 | 81 | 89 | 3.5 | 1.0 | A |
| 12 | 40 | 1 | 61 | 3 | 1931 | 1630 | 23 | 17 | 28 | 31 | 18 | 20 | 0.9 | 1.4 | A |
| 13 | 22 | 1 | 20 | 5 | 1177 | 1024 | 40 | 42 | 48 | 42 | 50 | 65 | 3.2 | 3.2 | A + C |
| 15 | 17 | 2 | 5 | 7 | 723 | 989 | 27 | 41 | 72 | 50 | 46 | 45 | 0.8 | 1.8 | A + D + C |
| 17 | 30 | 6 | 52 | 21 | 6680 | 8550 | 50 | 51 | 64 | 57 | 50 | 94 | 3.1 | 1.7 | A + C |
| 18 | 26 | 10 | 31 | 14 | 1146 | 1113 | 44 | 64 | 107 | 132 | 73 | 76 | 1.0 | 1.6 | A + C |
| 19 | 36 | 10 | 1 | 8 | 5046 | 3890 | 72 | 63 | 70 | 59 | 35 | 26 | 4.9 | 0.3 | A + B + C |
| 24 | 18 | 4 | 31 | 10 | 1395 | 1170 | 24 | 23 | 48 | 54 | 32 | 23 | 4.4 | 6.0 | A + C |
| 25 | 9 | 4 | 37 | 17 | 1843 | 2100 | 61 | 60 | 86 | 106 | 103 | 155 | 1.6 | 0.8 | A + C |
| 27 | 42 | 6 | 34 | 5 | 1546 | 2212 | 38 | 50 | 67 | 68 | 88 | 101 | 3.5 | 1.1 | A + D |
| 29 | 11 | 3 | 72 | 4 | 1060 | 1161 | 59 | 66 | 63 | 46 | 97 | 71 | 5.3 | 4.9 | A |

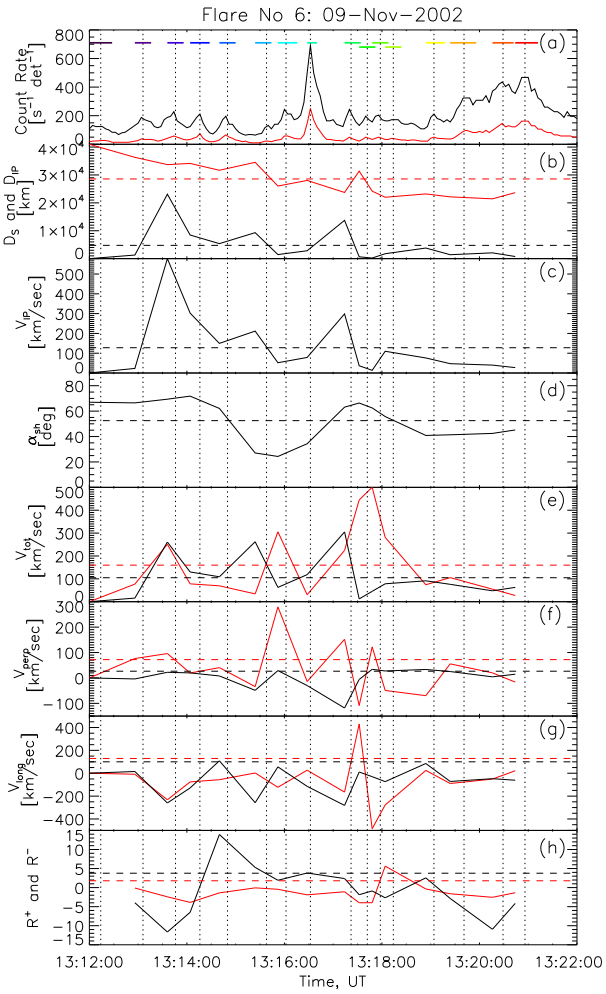


**Figure 7** Temporal variations of quantitative characteristics of paired HXR sources calculated for flare No. 6. (a) RHESSI corrected count rates in the 25 – 50 keV (black) and 50 – 100 keV (red) channels. The black vertical dotted lines show identified significant peaks. The colored horizontal segments at the top mark time intervals for which HXR images were synthesized (see Figures 5(b) and 6(a)). (b) $D_S$ (red) and $D_{IP}$ (black); (c) $V_{IP}$; (d) $\alpha_{sh}$; (e) $V^+$ (red) and $V^-$ (black); (f) $V_\perp^+$ (red) and $V_\perp^-$ (black); (g) $V_\parallel^+$ (red) and $V_\parallel^-$ (black); (h) $R^+$ (red) and $R^-$ (black). See Section 4.7 for an explanation of these notations. The horizontal dashed lines show the means of the presented characteristics in panels (b) – (e), while the means of the absolute values of the corresponding characteristics are shown in panels (f) – (h).

- The dimensionless parameters $R^+ = v_\parallel^+ / v_\perp^+$ and $R^- = v_\parallel^- / v_\perp^-$. These parameters provide information on which type of HXR source movement, along an MPIL or perpendicular to it, is more pronounced between two HXR peaks.

The time profiles of the parameters calculated for flare No. 6 are shown in Figure 7. The non-stationary pattern of all the calculated characteristics is evident. However, no obvious peak-to-peak correlation between HXR pulsations and the characteristics of the HXR source dynamics is seen. This indicates that these parameters of the HXR source dynamics are not linearly correlated with the HXR intensity or that the accuracy of measurements of these parameters is not sufficiently high.

We also calculated the mean values of these characteristics averaged over the significant peaks of each group 1 flare for which we had images of good quality. These mean values (placed in $\langle\rangle$ parentheses) and their standard deviations ($\sigma$) are summarized in Table 4. They provide a general view of the quantitative characteristics of the source dynamics of the HXR pulsations (with time differences in the range of $P \approx 8 – 270$ s) in flares.

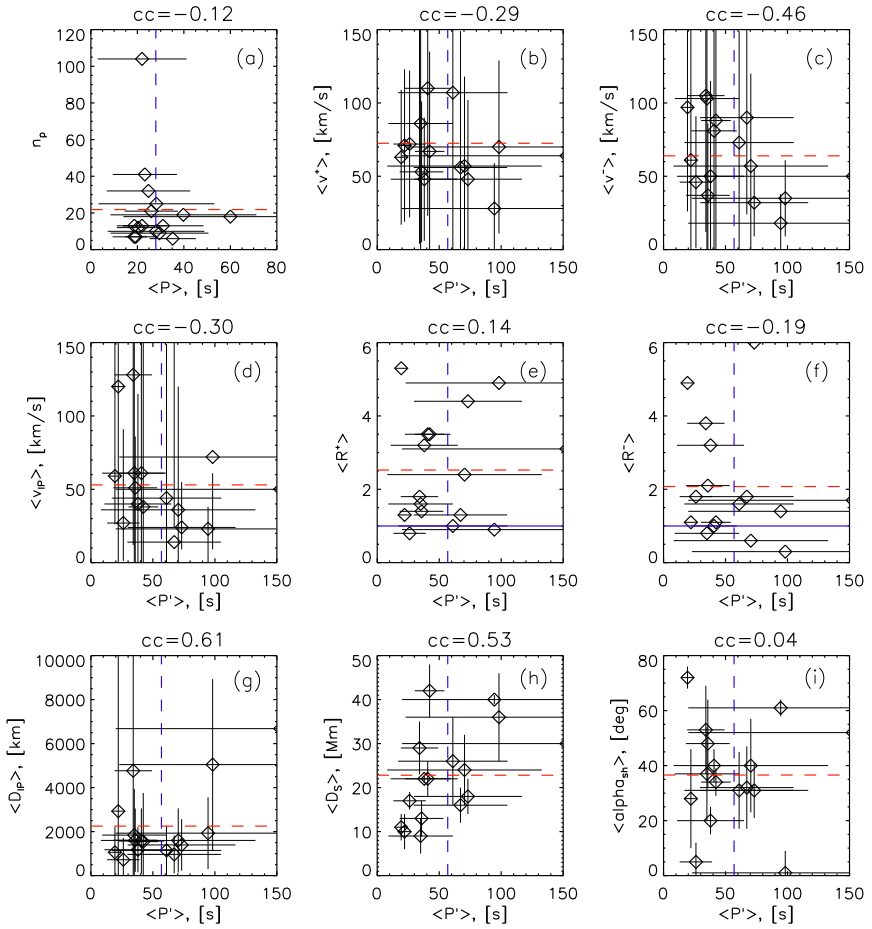


**Figure 8** Mean quantitative characteristics of the dynamics of the paired HXR pulsation sources calculated for group 1 flares (diamonds). Errors (standard deviations; see Table 4) are shown by black thin solid horizontal and vertical segments. The mean values of the characteristics, averaged over all flares, are shown by red horizontal and blue vertical dashed lines. The blue horizontal solid lines in panels (e) and (f) show the level of 1. The linear Pearson correlation coefficient (*cc*) calculated for each pair of the variables is shown at the top.

To explore the general picture of the calculated characteristics, we plotted them (Figure 8) *versus* the mean time differences, corrected by the special coefficient $r_p$, which is different for different flares, *i.e. versus* $\langle P' \rangle = \langle P \rangle r_p$. For a given flare this coefficient (column 15 in Table 2) is calculated as $r_p = n_p/k_p$, where $n_p$ is the number of all significant HXR peaks found in this flare (in the 50 – 100 keV band), and $k_p$ is the number of HXR pulsations of this flare for which we were able to reconstruct images of good quality that we then used to calculate the discussed characteristics. This coefficient is used to take into account that we were able to reconstruct images for only part of the significant peaks, and that times between successive images are not real times between successive peaks. We note that in Figure 8(a) we plot the numbers of all significant peaks ($n_p$) *versus* $\langle P \rangle$ (but not *versus* $\langle P' \rangle$ as in all other panels) because $n_p$ is calculated directly from RHESSI's corrected count rates as well as $\langle P \rangle$. For each pair of physical variables, shown in Figure 8, we calculated

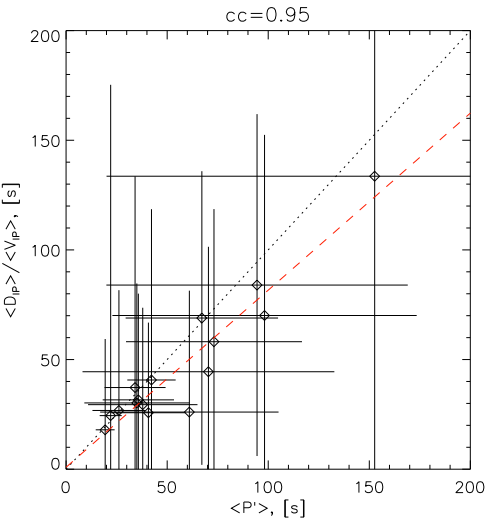


**Figure 9** Relation between the ratio $\langle D_{\rm IP}\rangle/\langle v_{\rm IP}\rangle$ and corrected mean time difference ($\langle P'\rangle$) for all group 1 flares (diamonds). The errors (standard deviations) are shown by the black thin solid horizontal and vertical segments. The black thin dotted line shows the line through the center of the coordinate system with the slope $k = 1$. The red dashed line shows the linear ($y = ax + b$) best fit of the data points with the slope $a = 0.81 \pm 0.18$ and $b = 0.89 \pm 11.64$. The linear Pearson correlation coefficient ($cc$) between $\langle D_{\rm IP}\rangle/\langle v_{\rm IP}\rangle$ and $\langle P'\rangle$ variables is shown at the top.

the linear Pearson correlation coefficient ($cc$). Its values are shown above the corresponding panels of Figure 8. In general, there is no strong linear correlation between the physical variables. Only $\langle D_{\rm IP}\rangle$ and $\langle D_{\rm S}\rangle$ show a significant positive correlation ($cc \approx 0.61$ and $cc \approx 0.53$, respectively) with $\langle P'\rangle$, indicating some links between distances between neighboring flaring loops (as well as their lengths) and the mean time differences of flare HXR pulsations.

However, the more important finding is the high correlation (the linear Pearson correlation coefficient is $cc \approx 0.95$) between the ratio $\langle D_{\rm IP}\rangle/\langle v_{\rm IP}\rangle$ and the corrected mean time difference $\langle P'\rangle$ (see Figure 9). The best fit of these data points with a linear function

$$\langle D_{\rm IP}\rangle/\langle v_{\rm IP}\rangle = a\langle P'\rangle + b \tag{1}$$

yielded $b = 0.89 \pm 11.64$ and the slope $a = 0.81 \pm 0.18$, which is close to 1 within the measurement error. The very high correlation between $\langle D_{\rm IP}\rangle/\langle v_{\rm IP}\rangle$ and $\langle P'\rangle$ may be caused by a combination of two causes. The first cause is methodological, since $v_{\rm IP}$ is calculated as the ratio between $D_{\rm IP}$ and a time difference between two corresponding peaks, *i.e.* $P$. However, this cannot be the only cause because we also found a high correlation between two independently determined variables $\langle D_{\rm IP}\rangle$ and $\langle P'\rangle$ (see Figure 8(g)). This indicates that there must be also a physical cause. We discuss this possibility in Section 5.4.

## 5. Summary of the Results and Their Discussion

Here we summarize and discuss the main observational results of our analysis of HXR sources in 29 investigated solar flares (see Table 1) that had a series of at least four successive HXR peaks (pulses or pulsations) in the four-second RHESSI-corrected count rates in the 50 – 100 keV channel. We would like to emphasize that since the criteria of flare selection were objective enough (see Section 3), the obtained results can most probably be generalized to all solar flares that display HXR pulsations, at least with characteristic time differences in the $P \approx 8 - 270$ s range.

### 5.1. Results of the Time-Sequence Analysis

We automatically identified significant peaks in the four-second RHESSI 50 – 100 keV (as well as 25 – 50 keV) background-subtracted corrected count rate data in the studied events. Their general characteristics are summarized in Table 2.

The total number of significant peaks in the studied flares varied from $n_{\mathrm{p}}^{\mathrm{min}} = 5$ to $n_{\mathrm{p}}^{\mathrm{min}} = 103$, with mean values of $\bar{n}_{\mathrm{p}}^{50} = 22$ and $\bar{n}_{\mathrm{p}}^{25} = 24$ in the 50 – 100 keV and 25 – 50 keV energy channels, respectively.

Time differences between successive peaks in the 50 – 100 keV channel varied between $P_{\mathrm{min}}^{50} = 8$ s and $P_{\mathrm{max}}^{50} = 224$ s, with a mean value of $\bar{P}^{50} = 27.1$ s averaged over all flares. In the 25 – 50 keV channel the situation is similar: $P_{\mathrm{min}}^{25} = 8$ s, $P_{\mathrm{max}}^{25} = 272$ s, and $\bar{P}^{25} = 23.0$ s, respectively.

Distributions of time differences combined for all 29 flares have rapidly decaying exponential form ($N(P) \sim \exp[-P/a_{\mathrm{p}}]$) with $a_{\mathrm{p}}^{50} = 17.78 \pm 0.11$ s in the 50 – 100 keV channel and $a_{\mathrm{p}}^{25} = 15.62 \pm 0.08$ s in the 25 – 50 keV channel (Figure 3). Maxima of these exponential distributions are close to the lower threshold level ($P_{\mathrm{thr}} = 8$ s) of time differences that can be identified, in principle, in time profiles with the 4-second step. This indicates clearly that the 4-second sampling is not enough to resolve the majority of peaks, whose time differences are below 8 s. This is an expected result. It is well known from higher cadence observations, made in particular with the CGRO/BATSE instrument, that distributions of widths (and, consequently, of time differences) of HXR pulses have decaying exponential form in the 0.3 – 3.0 s range (Aschwanden, Schwartz, and Alt, 1995). Thus, in the present work we are restricted to physical processes occurring in flare regions on time scales greater than $P_{\mathrm{min}} \approx P_{\mathrm{thr}} = 8$ s. This restriction is not due to the physics of flare processes. It is caused by the limited time resolution ($\mathrm{d}t = 4$ s) of the available data sets.

Individual distributions of time differences in the majority of inspected flares are similar in shape to the combined distributions (*cf.* Figures 2 and 3). They also have a decaying exponential form with maxima close to $P_{\mathrm{thr}} = 8$ s. However, we found that at least in three flares (No. 6, 12, and 23) distributions of time differences have bell-like shapes. They can be approximated (though not ideally) with Gaussian functions with positions of maxima and half-widths at half-maxima corresponding to average values and standard deviations of time differences. Moreover, we found that all time differences in these flares are within the $\langle P \rangle \pm 3\sigma_P$ range. This indicates that at least in these three flares the time differences between successive HXR peaks are random variables distributed normally around their own average values $\langle P \rangle$. We refer to the average value of all time differences in a given flare as the mean time difference. Physically, this is the most probable time interval between successive HXR peaks of a given flare. As in the majority of flares we only observed exponential tails of the time difference distributions and did not observe real maxima of these distributions (if they exist) because of the limited time resolution, we did not find real most probable time differences (*i.e.* true mean time differences) for the majority of flares. The mean time differences ($\langle P \rangle$) that we estimated are therefore more correctly treated as artificial (not true) characteristic time intervals between HXR peaks available for observations on the particular timescales between $P_{\mathrm{min}} \approx P_{\mathrm{thr}} = 8$ s and $P_{\mathrm{max}} \approx 270$ s.

It is worth mentioning that in the majority ($\approx 75$ %) of the studied flares more than half of the time differences are within the $\langle P \rangle \pm 0.5\langle P \rangle$ range (columns 5 and 10 in Table 2). Intuitively, this means that in these flares the spread of the time differences around their (artificial) mean values is not very high. This may be a signature of QPPs. However, this signature is not devoid of subjectivity and shortcomings; as discussed in Section 1, there is

no precise definition of what constitutes quasi-periodicity. In particular, it is not clear what exact percentage of pulsations in a given flare must be within this $\langle P \rangle \pm 0.5\langle P \rangle$ range to be treated as quasi-periodic ones. In addition, the range $\langle P \rangle \pm 0.5\langle P \rangle$ is chosen subjectively. We cannot strongly argue why the coefficient in the right hand side should be equal to 0.5 and not to some other values (see, *e.g.*, Jakimiec and Tomczak, 2013, for comparison).

On the other hand, we found from wavelet and periodogram analysis, taking into account the power-law (red noise) properties of the data (Vaughan, 2005; Gruber *et al.*, 2011; Inglis, Ireland, and Dominique, 2015), that HXR pulsations in the majority of the studied flares do not show quasi-periodicity (see Table 3). This finding is not consistent with the result discussed in the previous paragraph. It also differs from the recent results by Simões, Hudson, and Fletcher (2015). However, our approach to the data analysis is not identical with the approach of Simões, Hudson, and Fletcher (2015), who used the time-derivatives of GOES soft X-ray data for the wavelet analysis. We performed the wavelet and periodogram analysis of the slightly altered RHESSI-corrected count rates in the 50 – 100 keV channel. We only subtracted pre-flare background levels and normalized the corrected count rates to their maxima in the time interval studied. We used this approach to modify the original data as little as possible. We also need to mention that our sample of flares differs from the sample of flares studied by Simões, Hudson, and Fletcher (2015). It follows from this that the result of finding a quasi-periodicity in the flare HXR data strongly depends on the chosen approach. This problem is non-trivial and requires further and deeper study, which is beyond the scope of the present article (see, *e.g.*, Nakariakov *et al.*, 2010; Gruber *et al.*, 2011; Inglis, Ireland, and Dominique, 2015, for further discussions). The investigation of quasi-periodicity in the studied flares is not the main goal of the present work. Instead, our aim is to investigate the dynamics of HXR pulsation sources in flaring regions, regardless of whether pulsations are quasi-periodic.

### 5.2. Results of the Dynamics Analysis of the HXR Sources

We investigated the spatio-temporal evolution of HXR sources relative to MPILs in the parent active regions of all 29 studied flares. Owing to the low signal-to-noise ratio and some other instrumental limitations, we were unfortunately unable to identify the positions of HXR sources of all significant peaks found in the time profiles of the HXR emission. Nevertheless, we did this for almost half of the peaks of each flare (see column 12 of Table 2). The average ratio of all significant HXR peaks of each flare ($n_\mathrm{p}$) to HXR peaks, for which we were able to determine the positions of the HXR sources ($k_\mathrm{p}$), is $\langle r_\mathrm{p} \rangle = \langle n_\mathrm{p}/k_\mathrm{p} \rangle \approx 2.2$. This is, in principle, enough to conclude in general about the dynamics of the HXR pulsation sources (with time differences $P \approx 8 – 270$ s) in flares.

First of all, we found that in all the studied flares the HXR sources were not stationary. The positions of the HXR sources of each subsequent pulsation differed from the positions of the HXR sources of previous pulsations, *i.e.* the HXR emission sources showed apparent movement (displacement) in the parent active regions from pulsation to pulsation. Generally speaking, this is an expected result because the motion of solar flare HXR sources is a well-known and common phenomenon (*e.g.*, Sakao, Kosugi, and Masuda, 1998; Bogachev *et al.*, 2005; Ji *et al.*, 2006; Gan, Li, and Miroshnichenko, 2008; Yang *et al.*, 2009). However, most previous works were not specifically concerned with the spatio-temporal evolution of the HXR pulsation sources. As far as we know, our study is the first such systematic (based on a large number of flares) investigation focused on the source dynamics of HXR pulsations. Since the sample of the studied flares is large and almost unbiased, we can conclude with

high confidence that HXR pulsation sources, at least with time differences $P \approx 8-270$ s, change their location from pulsation to pulsation in virtually all solar flares.

Second, we found that all flares can be subdivided into two nominal groups based on the character of the source dynamics of the HXR pulsation. Group 1 flares (55 % of all events; see column 11 of Table 1) showed systematic dynamics of HXR sources from pulsation to pulsation with respect to a single MPIL with a relatively simple extended shape in the photosphere. By systematic dynamics we mean one of the standard types of HXR source motions or their combinations (*e.g.*, Bogachev *et al.*, 2005; Yang *et al.*, 2009). We found (see columns 14 – 16 of Table 4) that the most common type of motion, present in almost all flares, is the parallel motion of paired HXR sources along a MPIL in the same direction. We also found that different types of motion were manifested simultaneously or in different time intervals during the majority of events. This is also a known phenomenon (Gan, Li, and Miroshnichenko, 2008; Yang *et al.*, 2009). Group 2 flares (45 % of all events) showed more chaotic displacements of HXR sources with respect to MPILs with more complex structure. Sometimes, several MPILs were present in the parent active regions of these flares.

We need to emphasize here that subdivision of flares into these two groups is quite subjective and conditional. In some cases, it was difficult to decide unambiguously to which group we must attribute a flare. Most probably, there is no principal difference between the physical mechanisms underlying the pulsatory energy release processes in flares of the two groups. We found that the temporal characteristics in the two groups of flares are very similar to each other. Probably, the only difference that may exist between the flares of group 1 and group 2 is the complexity of the magnetic geometries in their parent active regions.

Based on these observations, we suggest that the mechanism of HXR pulsations (at least with time differences of the considered range $P \approx 8-270$ s) in the two groups of flares is related to successive ignition or triggering of energy release process and acceleration (injection) of electrons in different magnetic loops (or bundles of loops). The group 1 flare regions consist of loops stacked into magnetic arcades that extend along an MPIL. The group 2 flare regions have more complex magnetic structures, and loops are arranged more chaotically and randomly relative to each other and to multiple MPILs. Cartoons summarizing observations of group 1 and group 2 flares are shown in Figure 10. These ideas are not new. They are based on the early works of de Jager and his colleagues (*e.g.*, van Beek, de Feiter, and de Jager, 1974a,b; de Jager and de Jonge, 1978; de Jager, 1979).

Because of the relative simplicity of the magnetic geometry, it was possible to investigate the dynamics of paired HXR sources of pulsations in group 1 flares in more detail than in group 2 flares. In particular, for each group 1 flare we estimated distances ($D_{\rm IP}$) between successively flaring loops of magnetic arcades and velocities ($v_{\rm IP}$) of a hypothetical trigger, which could cause initiation of energy release and acceleration (injection) of electrons in the loops. In each flare $D_{\rm IP}$ and $v_{\rm IP}$ have different values for different pulsations (see columns 6 – 7 and 8 – 9 of Table 4). The mean values of these physical parameters, averaged over all flares, are $\bar{D}_{\rm IP} \approx 2250$ km and $\bar{v}_{\rm IP} \approx 53\,{\rm km\,s^{-1}}$. These values are consistent with values estimated in some previous case studies (*e.g.*, Grigis and Benz, 2005; Zimovets and Struminsky, 2009; Inglis and Dennis, 2012).

However, in our opinion, the more interesting and physically important finding is the high linear correlation between the ratio of mean values $\langle D_{\rm IP}\rangle$ and $\langle v_{\rm IP}\rangle$ (for each flare) and the corrected mean time difference $\langle P'\rangle = \langle P\rangle r_{\rm p}$ (see Figure 9 and Equation (1)). The linear slope ($a = 0.81 \pm 0.18$) between $\langle D_{\rm IP}\rangle/\langle v_{\rm IP}\rangle$ and $\langle P'\rangle$ variables is close to unity within the measurement errors. This means that the characteristic time between successive pulsations, identified in the light curves of flare HXR emission (*i.e.* its mean time difference), is equal to the characteristic time required for an energy release trigger to propagate from one flaring

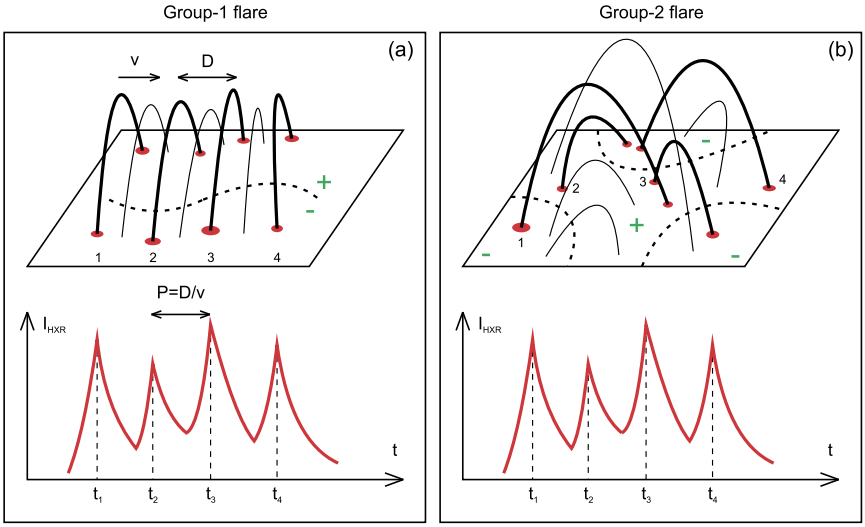


**Figure 10** Cartoons generalizing observations of group 1 (a) and group 2 (b) flares. (*Top*) Morphology of the flaring regions. The thick solid arc-shaped curves show flaring loops with HXR sources in their footpoints (red ellipses). The thin solid arc-shaped curves show non-flaring loops, *i.e.* loops without detectable HXR emission. MPILs are shown by the dashed curves. Signs of magnetic polarity are marked with green + and − symbols. (*Bottom*) Time profiles of detected flare HXR emission.

loop (bundle of loops) to the next (see Figure 10). The main question that remains is what triggers the energy release.

### 5.3. Erupting Flux-Rope as a Possible Trigger of Energy Release

It is generally accepted that energy release in flares is related to the process of magnetic reconnection (*e.g.*, Priest and Forbes, 2002; Somov, 2007; Shibata and Magara, 2011). However, the trigger of magnetic reconnection and flare energy release is not well known as yet and is a matter of active debate. Many models were proposed to explain the pulsatory (bursty) character of energy release processes in flares (see, *e.g.*, Zaitsev and Stepanov, 2008; Nakariakov and Melnikov, 2009; Nakariakov *et al.*, 2016; and references therein). It is not our goal to discuss the applicability of all these models to the observational results we found in the current study. Here we briefly discuss only one possible interpretation, which is well consistent with the observations discussed above.

We found that at least 88 % of group 1 and 85 % of group 2 flares were accompanied by CMEs (see column 12 of Table 1). The apparent absence of CMEs in the remaining 12 % – 15 % of flares might be due to the location of parent active regions close to the solar disk center, according to our selection of the flares (see column 10 of Table 1). It might be difficult to detect some weak and narrow CMEs, which started from parent active regions located close to the solar disk center and propagated toward the observer. We also recall that $\approx$20 % of the eruptions do not lead to CMEs (*e.g.*, Schmieder, Démoulin, and Aulanier, 2013). It is therefore possible that at least some of the flares in which no CME was detected might also be eruptive events. Thus, the majority of the studied flares were eruptive events. Eruptive flares are related to destabilization and ejection of magnetic flux ropes from parent active

regions (*e.g.*, Schrijver, 2009; Schmieder, Démoulin, and Aulanier, 2013). Regardless of the magnetic geometry of the parent active regions, whether they are quasi-bipolar or multi-polar, the process of flux rope eruption is associated with the interaction of the magnetic field of a flux rope with the surrounding magnetic field. Since a flux rope has an elongated shape, it can interact with different surrounding magnetic flux tubes (loops) of a parent active region at different times when erupting because the surrounding magnetic field is non-homogeneous and, consequently, the process of eruption can be non-uniform along the axis of a flux rope. The interaction of different parts of a flux rope with different surrounding magnetic flux tubes (loops) at different times can lead to a sequence of episodes of magnetic reconnection and acceleration of electrons in different places and, as a result, to a sequence of HXR peaks (pulsations) and apparent displacement of HXR sources from pulsation to pulsation. If a parent active region has, in general, a quite simple quasi-bipolar magnetic configuration with an elongated MPIL (see Figure 10(a) for a cartoon of this situation), then the eruption of a flux rope can be whipping-like or zipping-like (*e.g.*, Grigis and Benz, 2005; Liu, Alexander, and Gilbert, 2009). This can explain group 1 flares. If a parent active region has more complex multi-polar magnetic structure with several MPILs, then an erupting flux rope will interact at different times with different loops oriented more randomly than in the case of a quasi-bipolar active region. Thus, the apparent displacements of HXR pulsation sources will have a more chaotic character in this case (see Figure 10(b) for a cartoon of this situation). This can explain group 2 flares.

The natural question is why some loops of the parent active regions produce significant HXR peaks while others do not. We do not know the precise answer to this question. We suggest that (a) different loops of an active region initially contain different amounts of energy, which can be released during interaction with a flux rope, and (b) the physical conditions in some loops are more favorable for a realization of more energy and/or for more efficient electron acceleration during interaction with a flux rope than in other loops. This is quite reasonable because we found from the observations that the physical characteristics of different flaring loops (such as their shear angle and length) differ quite significantly from each other. Moreover, an interesting question is what determines the observed characteristic spatial scale ($\bar{D}_{\mathrm{IP}} \approx 2250$ km; see Figure 8(g)) between the observed neighboring flaring loops. Is this related to some characteristic spatial scale of the magnetic field in the photosphere, *e.g.*, the scale of solar granules (*e.g.*, Nordlund, Stein, and Asplund, 2009, and references therein), or is it merely a consequence of the limited angular resolution of RHESSI ($d \approx 2.3''$, which corresponds to $\approx 1670$ km)? These questions require further study, which is beyond the scope of the present paper.

It is worth noting that the slipping reconnection (Priest and Démoulin, 1995; Aulanier *et al.*, 2006) could be a natural part of the scenario discussed above. It was shown by 3D MHD simulations (Janvier *et al.*, 2013) and with observations of a real X-class flare (Dudík *et al.*, 2014) that slipping reconnection, associated with an eruption of a flux rope, can be responsible for an apparent motion in the footpoints of hot flare loops along flare ribbons with velocities of several tens of $\mathrm{km\,s^{-1}}$. These velocities are consistent with the characteristic velocities of an apparent motion of the HXR pulsation sources (see Table 4). The recent observational indication that the quasi-periodic regime of the slipping reconnection might exist during an X-class flare is also interesting in this context (Li and Zhang, 2015). In principle, this regime of slipping reconnection could be responsible for the flare QPPs (see also Section 5.4). However, since there is no direct observational evidence of the link between slipping reconnection and the HXR pulsations, we do not discuss this subject in more detail here. It requires further more detailed observations and simulations.

### 5.4. On the Quasi-periodicity of HXR Pulsations

Finally, we touch on the problem of the quasi-periodicity of flare pulsations.

Although there is no generally accepted definition of the quasi-periodicity of flare emission, intuitively it means that the times between emission peaks are not very different from each other. In the terminology of our article this means that for a given flare all significant time differences ($P$) are almost the same and, thus, they are approximately equal to the mean time difference $\langle P \rangle$. In turn, we found from the observations (see Section 4.7) that $\langle D \rangle / \langle v \rangle \approx \langle P \rangle$, where $\langle D \rangle$ and $\langle v \rangle$ are the mean values of the distances between neighboring flaring loops and the speed of a flare trigger, respectively, averaged over all HXR peaks of a flare. Consequently, the quasi-periodicity means that the ratio $D/v \approx \langle P \rangle \approx const$ for all peaks, *i.e.* the ratio $D/v$ can be considered as a kind of quasi-invariant for a given flare. In particular, this can be realized when distances between neighboring flaring loops are almost the same and a trigger (*i.e.* a flux-rope) moves with almost constant speed along an MPIL. Obviously, in natural magnetic systems such as a real flare region with an erupting flux-rope this situation is quite specific and probably not very common. This is the reason why the quasi-periodicity of HXR pulsations is not found in all flares (see Table 3).

## 6. Conclusions

We performed a systematic analysis of the spatio-temporal evolution of sources of hard X-ray (HXR) pulsations in solar flares. Our study was focused on the disk flares whose impulsive phases were accompanied by a series of more than three successive peaks (pulsations) of HXR emission detected in RHESSI's four-second background-subtracted corrected count rates in the 50 – 100 keV channel. Out of 154 such pre-selected flares detected by RHESSI from February 2002 to June 2015 with characteristic time differences between successive peaks $P \approx 8 – 270$ s, we studied 29 events with the best quality of the available data sets.

The main observational result of our analysis is that the sources of HXR pulsations in all studied flares were not stationary; they showed apparent movements in the parent active regions from pulsation to pulsation. We found that flares can be subdivided into two nominal groups depending on the character of the HXR source dynamics. Group 1 consists of 16 flares (55 %) with systematic dynamics of the HXR sources from pulsation to pulsation with respect to an MPIL with a simple extended shape at the photosphere. Group 2 consists of 13 flares (45 %) with more chaotic displacements of the HXR sources with respect to an MPIL with a more complex structure, and sometimes several MPILs were present in the parent active regions of such flares.

Based on the observations, we concluded that the mechanism of flare HXR pulsations (at least with time differences of the considered range, *i.e.* $P \approx 8 – 270$ s) is related to successive triggering of the flare energy release process in different magnetic loops (or bundles of loops) of the parent active regions. Group 1 flare regions consist of loops stacked into magnetic arcades extended along an MPIL. Group 2 flares have more complex magnetic structures and the loops are arranged more chaotically and randomly there. We would like to emphasize that the flare pulsation models that are based on magnetic loop oscillations do not explain the observational results.

We also found that at least 14 (88 %) group 1 flares and 11 (85 %) group 2 flares were accompanied by CMEs, *i.e.* the majority of the flares studied were eruptive events. This strongly indicates that eruptive processes play a significant role in the generation of HXR

pulsations in flares. We discussed the possibility that an erupting flux rope acts as a trigger of flare energy release. If it interacts successively with different loops of a parent active region, then this can lead to the apparent motion of HXR sources and to a series of HXR pulsations. However, the exact mechanisms responsible for the pulsations (and their quasi-periodic character in some flares) remain unclear at present and require further more detailed investigations.

**Acknowledgements** We thank V.M. Nakariakov, V.F. Melnikov, S.A. Anfinogentov, E.P. Kontar for helpful discussions, E.G. Kupriyanova for help with the wavelet analysis, A.R. Inglis for help with the English. We would like to acknowledge the anonymous referee for useful comments that helped to improve the manuscript. We are grateful to the spacecraft teams and consortia (RHESSI, SOHO/MDI, SOHO/LASCO, SDO/HMI, GOES) and ground-based observatories (RSTN, e-Callisto) whose data were used in this study. This study was supported by the Russian Foundation for Basic Research (grants No. 16-02-00328, 16-32-00535, 15-32-50998, 15-32-21078, 14-02-00924) and by the Marie Curie FP7 PIRSES-GA-2011-295272 "RadioSun" Project. We are also grateful to the Specialized Research Fund for State Key Laboratories of China.

**Disclosure of Potential Conflicts of Interest** The authors declare that they have no conflicts of interest.

## Appendix A: HXR Light Curves, Pulsations, and Time Differences Between Successive Pulsations of the Studied Flares

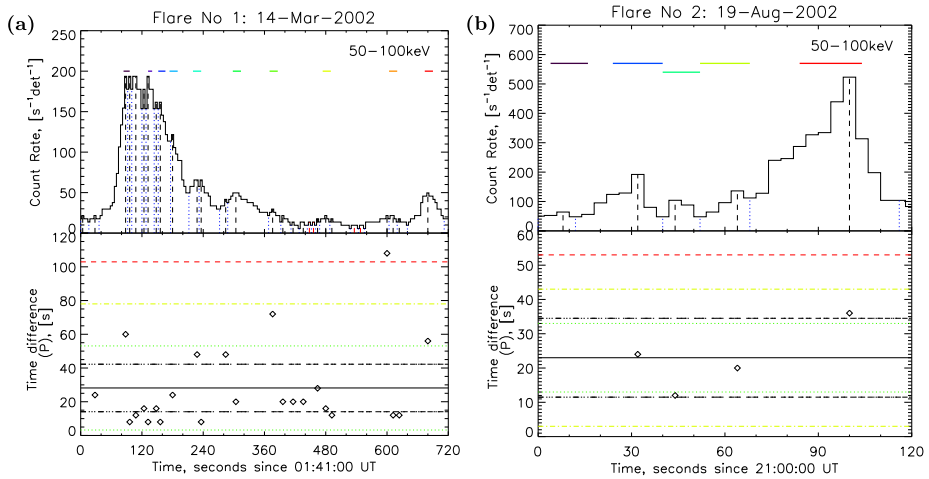


**Figure 11** Peaks and time differences in the RHESSI 50 – 100 keV corrected count rates in flares No. 1 – 5 and 7 (see Table 1). (*Top*) The RHESSI four-second background-subtracted corrected count rate in the 50 – 100 keV channel is shown by the black curve. The black and red vertical dashed lines indicate significant and insignificant local maxima. The blue vertical dotted lines indicate local minima. The color horizontal segments at the top mark time intervals for which HXR images were synthesized for further analysis (see Figures 2 – 8). (*Bottom*) Time differences between successive significant peaks are shown by diamonds. The average value of all time differences $\langle P \rangle$ is shown by the black horizontal solid line. The black, green, yellow, and red horizontal dashed and dotted lines indicate levels $\langle P \rangle \pm 0.5\langle P \rangle$, $\langle P \rangle \pm 1.0\sigma_{\langle P \rangle}$, $\langle P \rangle \pm 2.0\sigma_{\langle P \rangle}$, and $\langle P \rangle \pm 3.0\sigma_{\langle P \rangle}$, respectively, where $\sigma_{\langle P \rangle}$ is the standard deviation of the time differences.

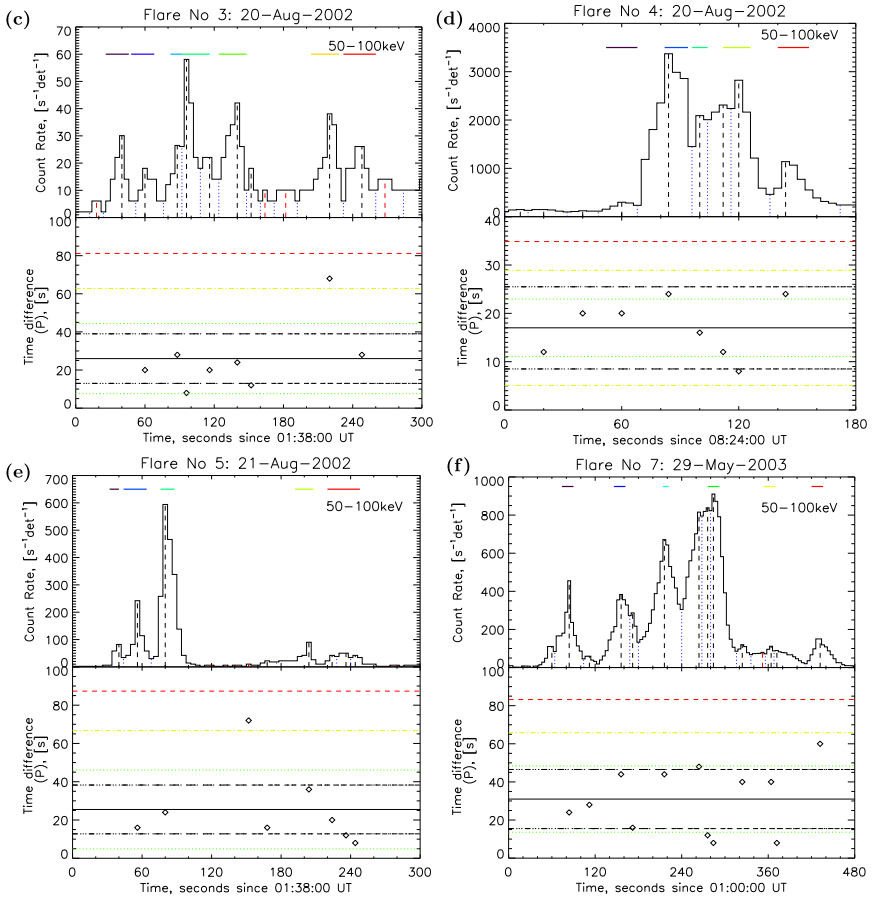


**Figure 11** (*Continued.*)

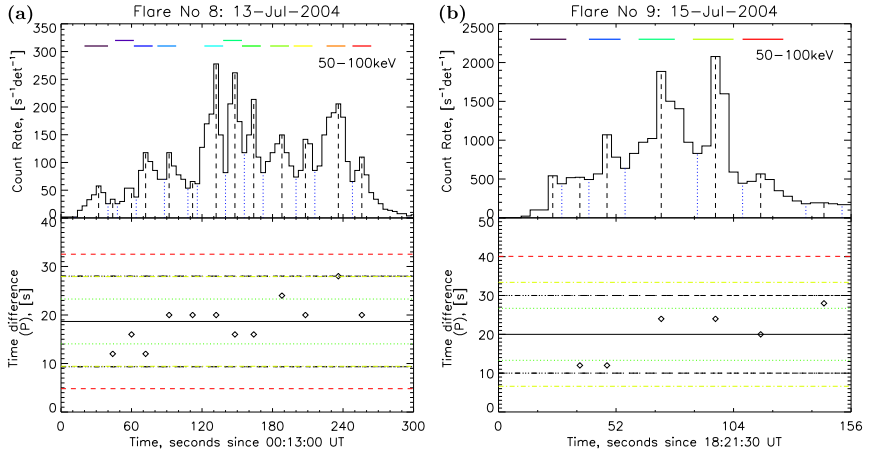


**Figure 12** Peaks and time differences in the RHESSI 50 – 100 keV corrected count rates in flares No. 8 – 15 (see Table 1). The panel content and drawing convention are the same as in Figure 11.

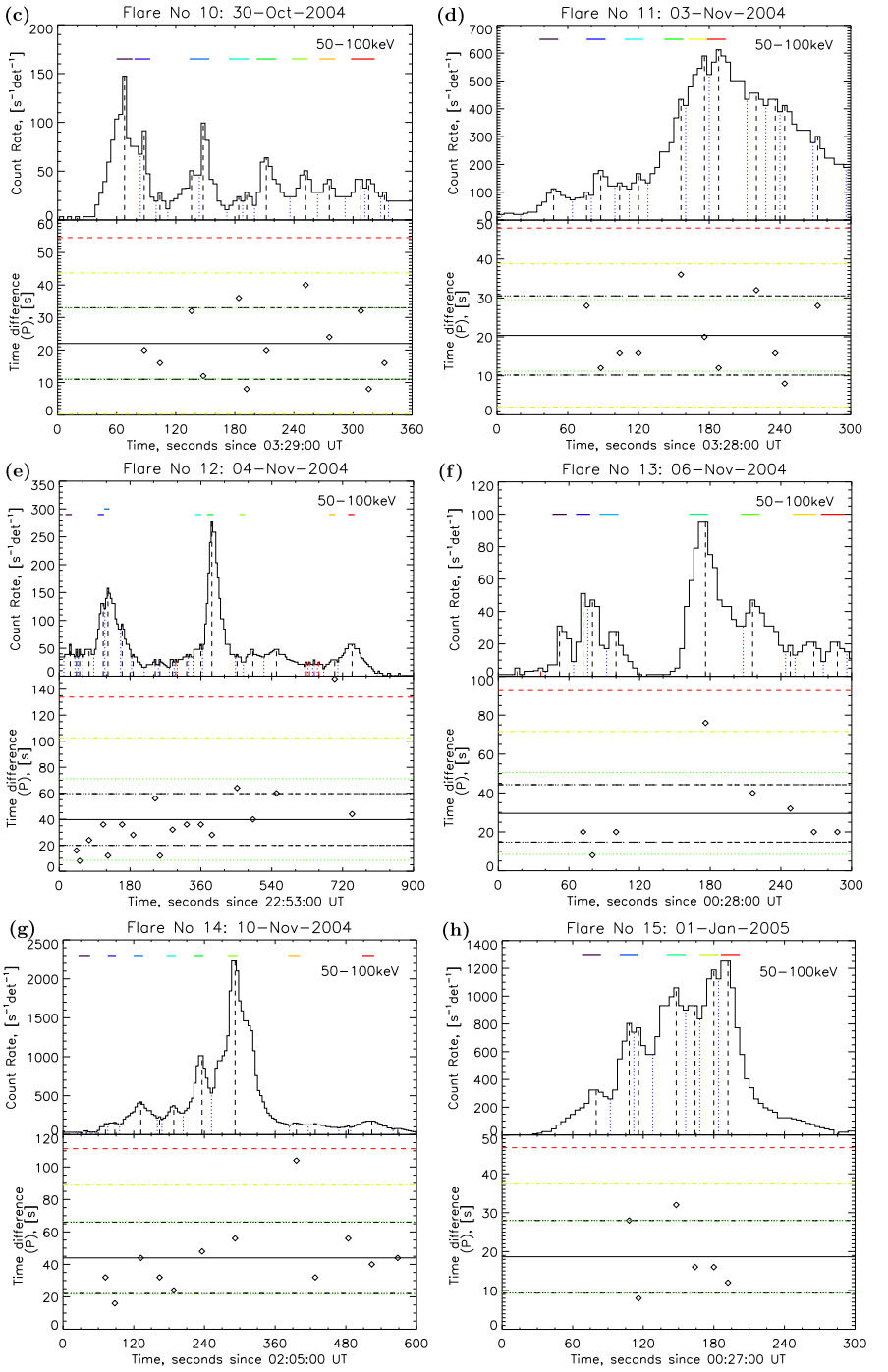


**Figure 12** (*Continued.*)

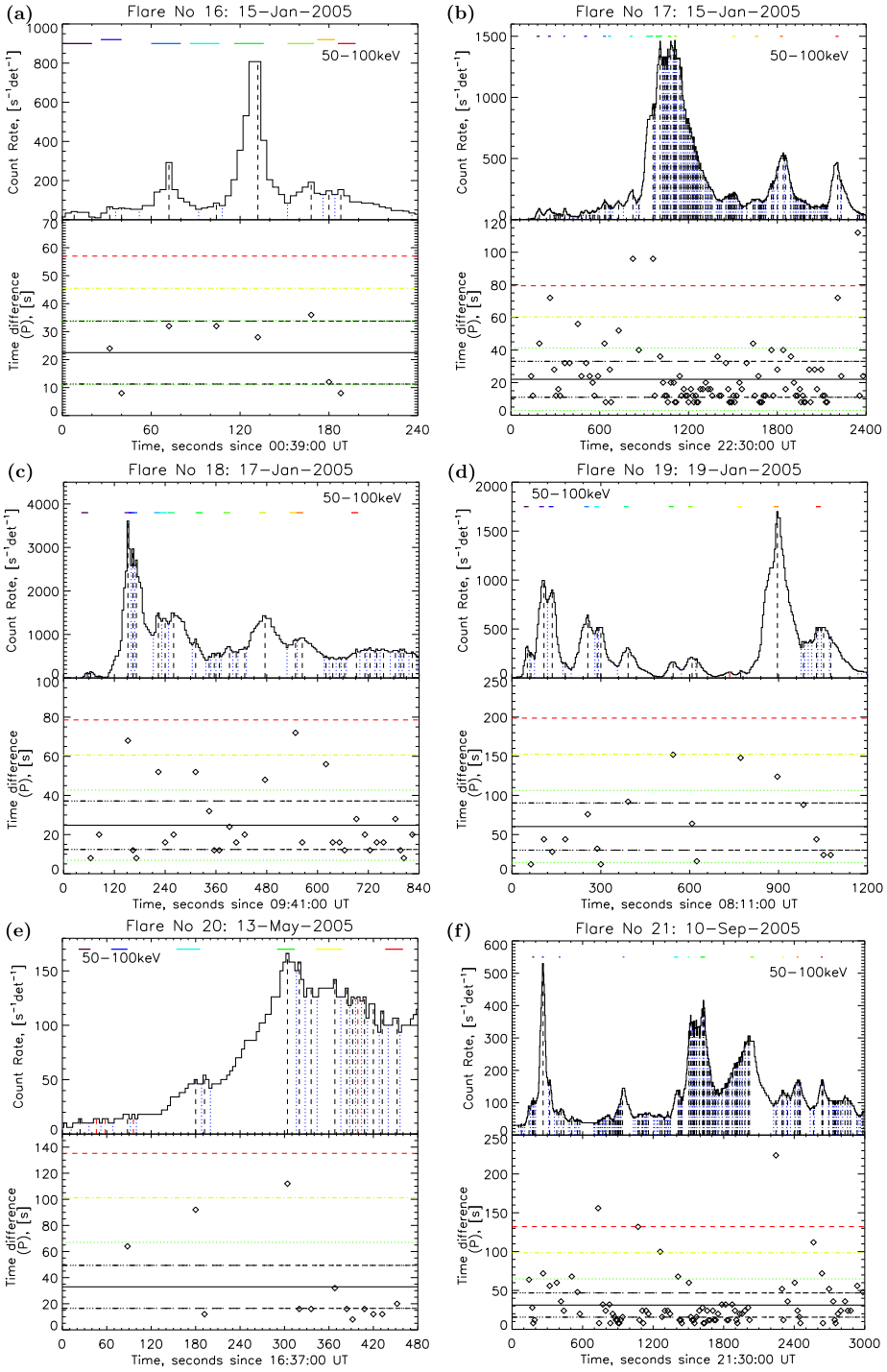


**Figure 13** Peaks and time differences in the RHESSI 50 – 100 keV corrected count rates in flares No. 16 – 23 (see Table 1). The panel content and drawing convention are the same as in Figure 11.

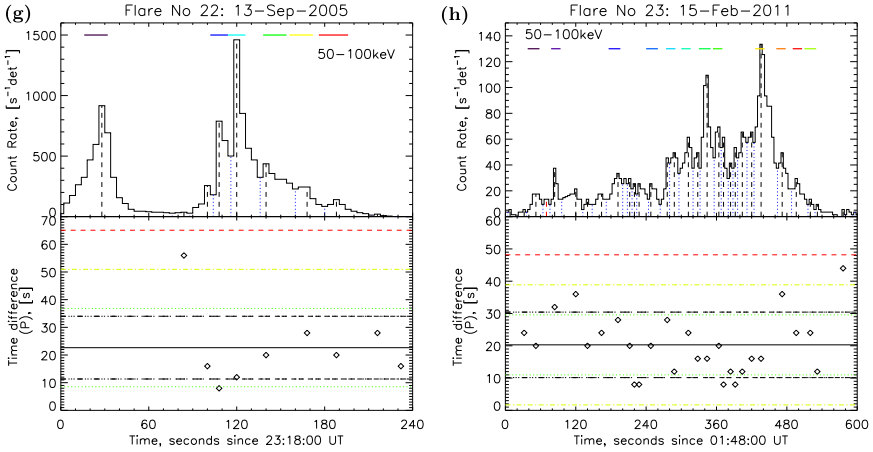


**Figure 13** (*Continued.*)

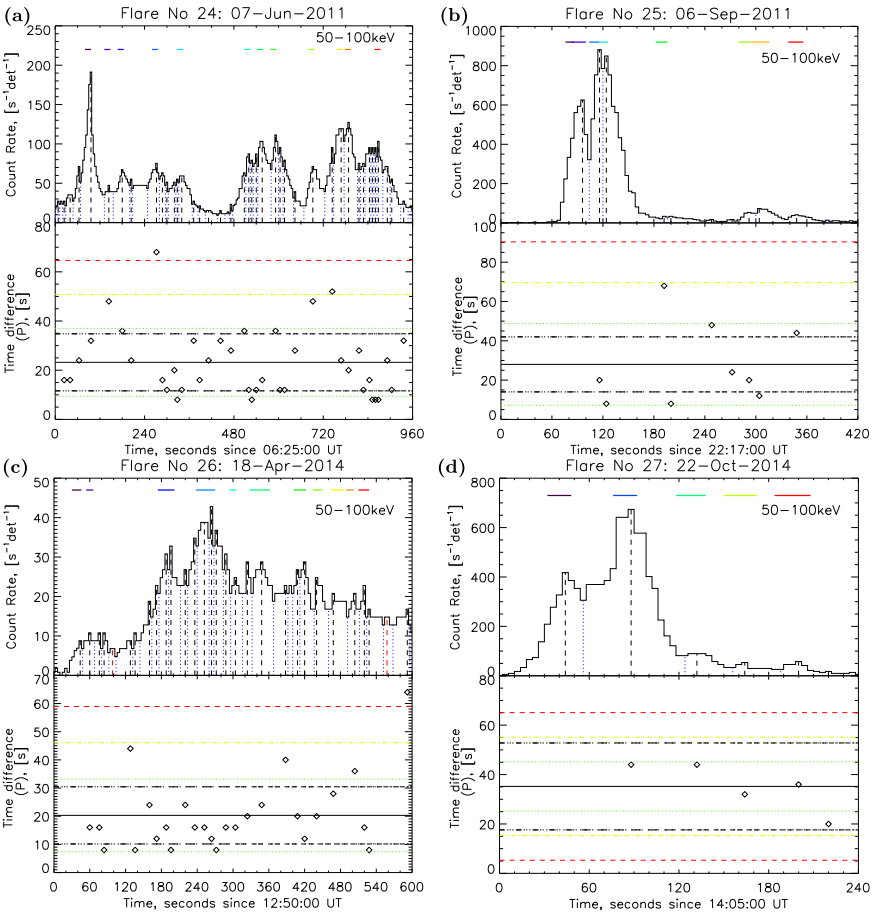


**Figure 14** Peaks and time differences in the RHESSI 50 – 100 keV corrected count rates in flares No. 24 – 29 (see Table 1). The panel content and drawing convention are the same as in Figure 11.

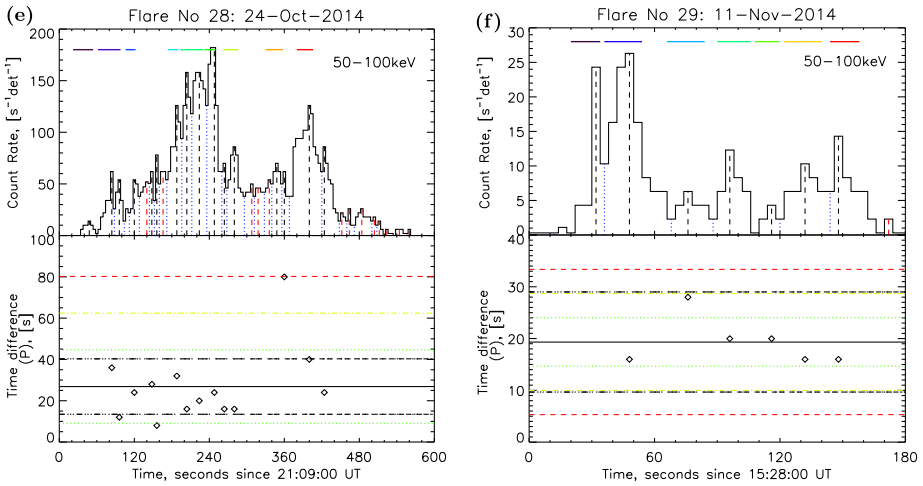


**Figure 14** (*Continued.*)

## Appendix B: Spatio-temporal Evolution of the Sources of the HXR Pulsations in the Studied Flares

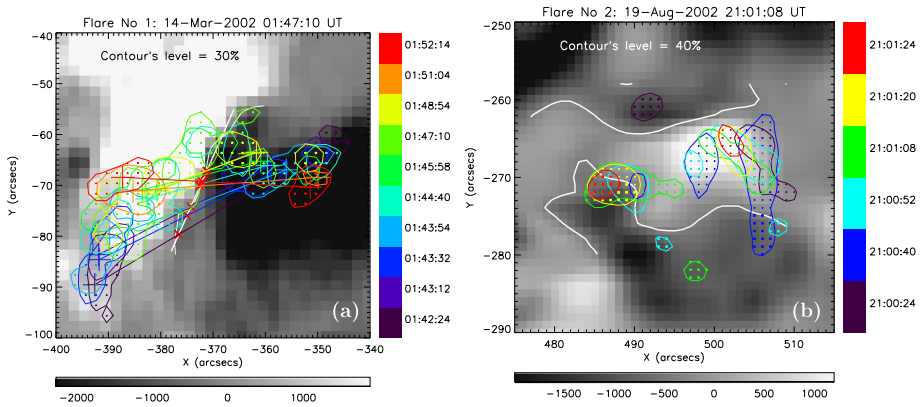


**Figure 15** Spatio-temporal evolution of the HXR pulsation sources in flares No. 1 – 5 and 7. The PIXON algorithm was used to reconstruct the HXR sources. The date and time of flare are shown above. The background images are the photospheric line-of-sight magnetograms obtained with the SOHO/MDI or SDO/HMI. The magnetic field color bars (in gauss) are presented below. The colors of the HXR sources correspond to the times of the HXR peaks shown near the color bars to the right. The contour levels of the HXR sources are labeled in the images. The large color crosses show the average positions (centroids) of the HXR sources at the corresponding times. The linear sizes of these crosses are equal to twice the FWHM of the RHESSI collimator number 1. The straight color lines connect paired HXR sources located in opposite magnetic polarities. The small red crosses indicate intersection points of these lines with the model MPIL (thick white lines). The real MPILs found from the magnetograms are shown as the thin white curves.

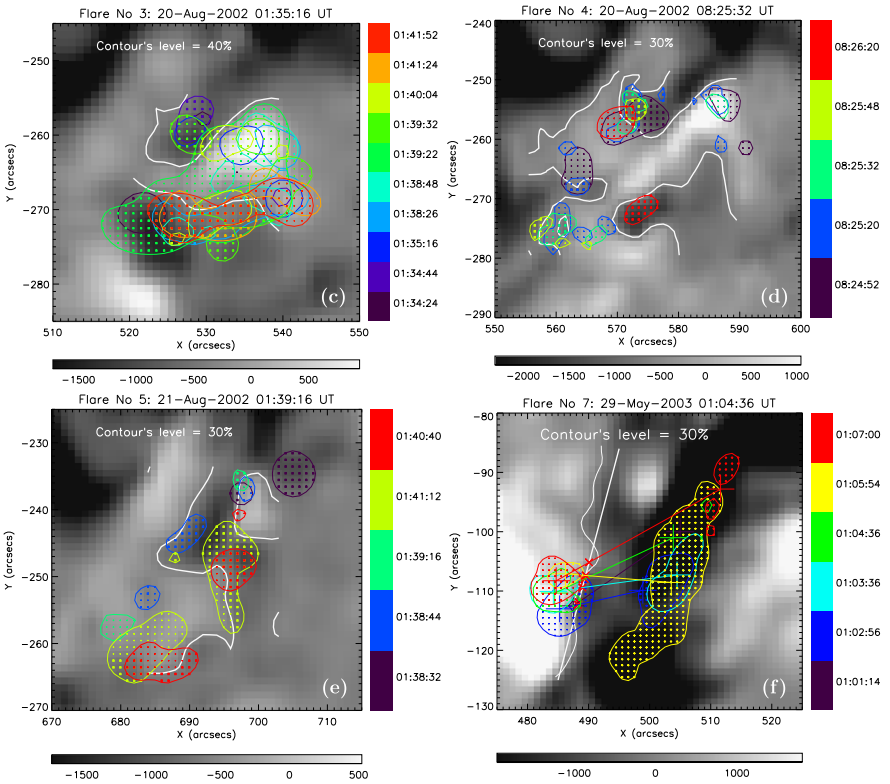


**Figure 15** (*Continued.*)

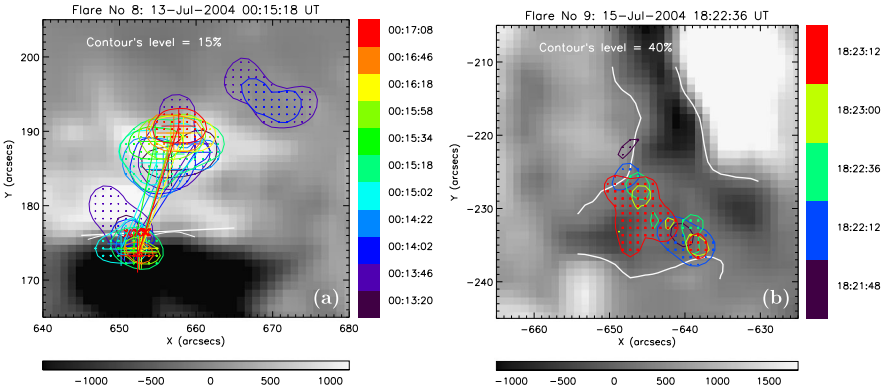


**Figure 16** Spatio-temporal evolution of the sources of the HXR pulsations in flares No. 8 – 15. The method and convention are the same as in Figure 15.

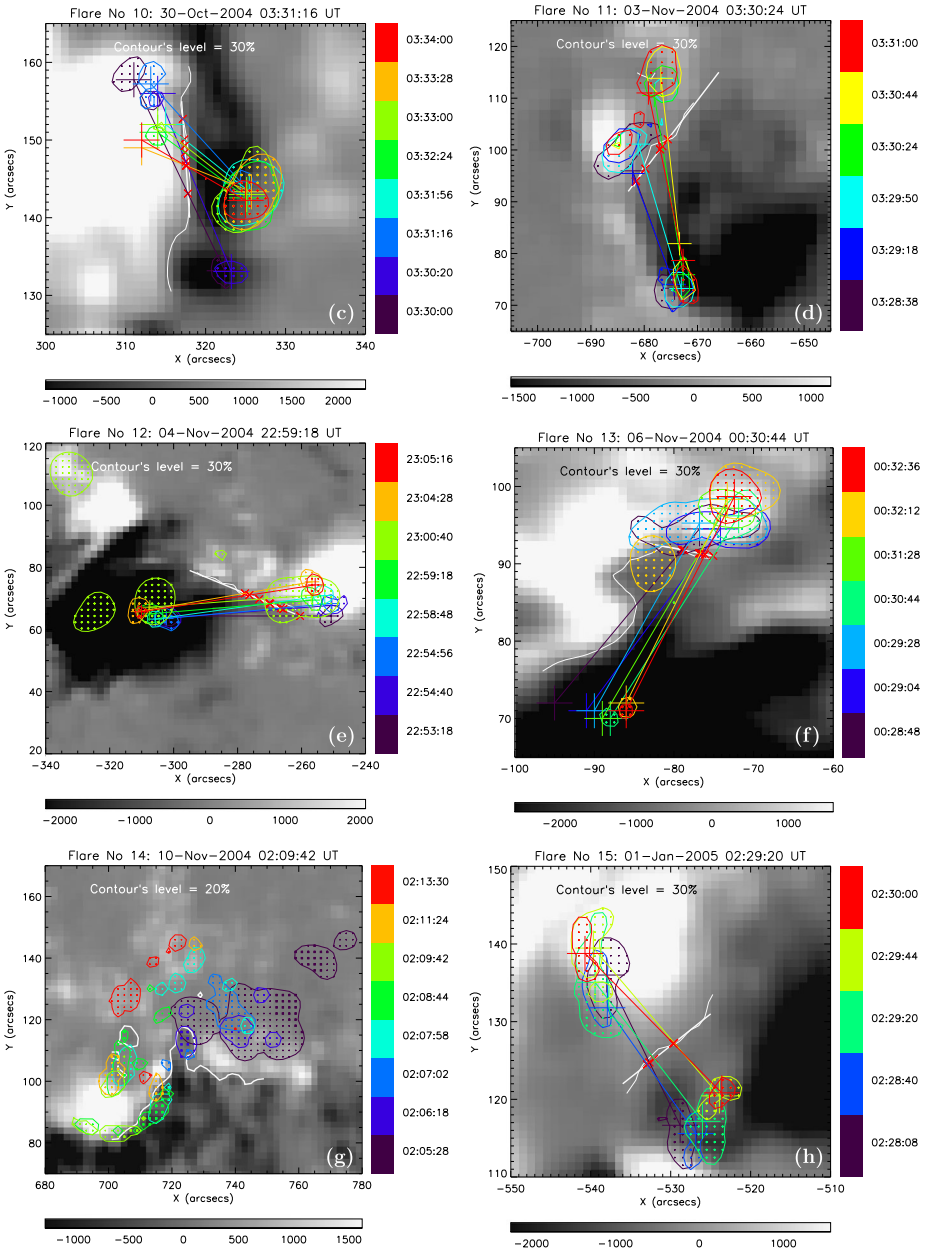


**Figure 16** (*Continued.*)

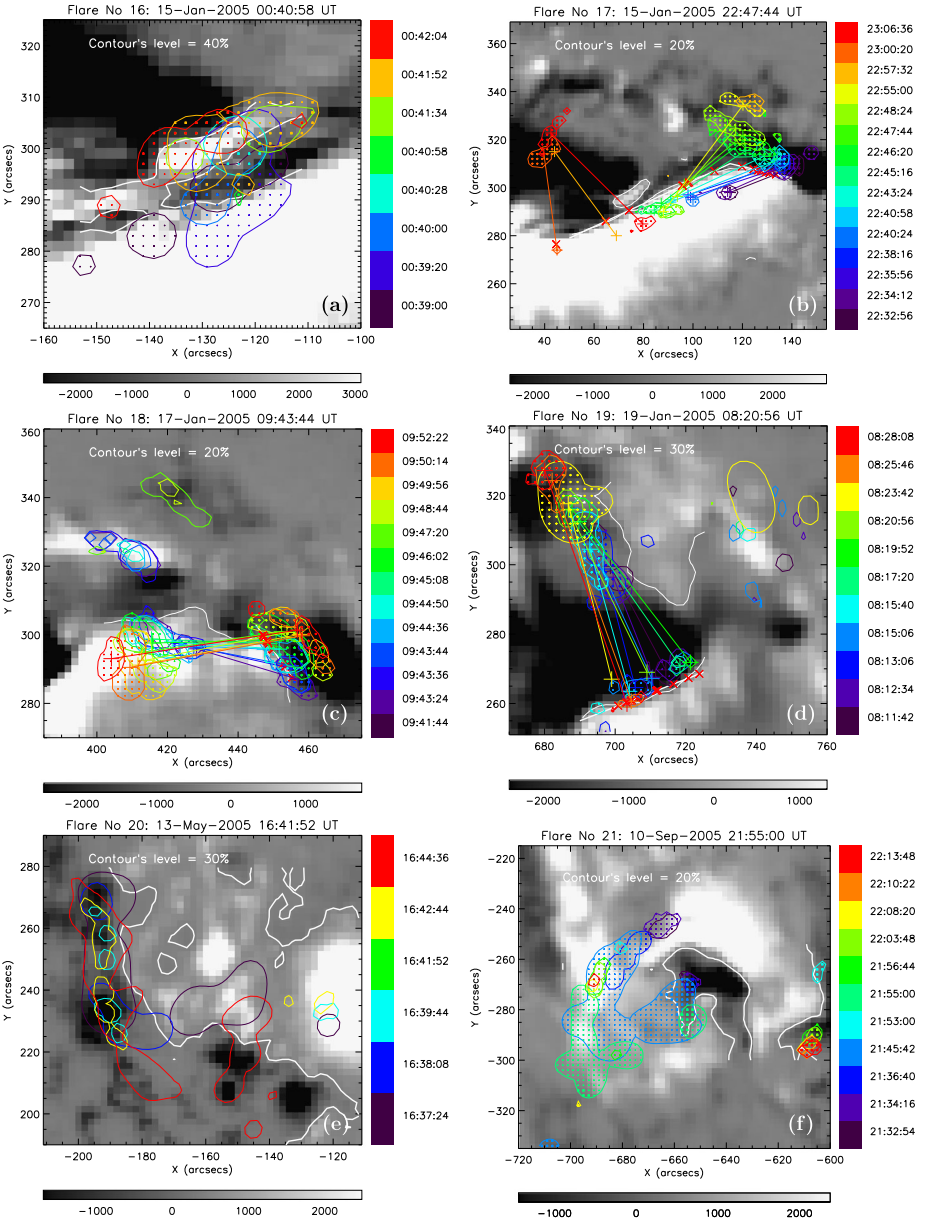


**Figure 17** Spatio-temporal evolution of the sources of the HXR pulsations in flares No. 16 – 23. The method and convention are the same as in Figure 15.

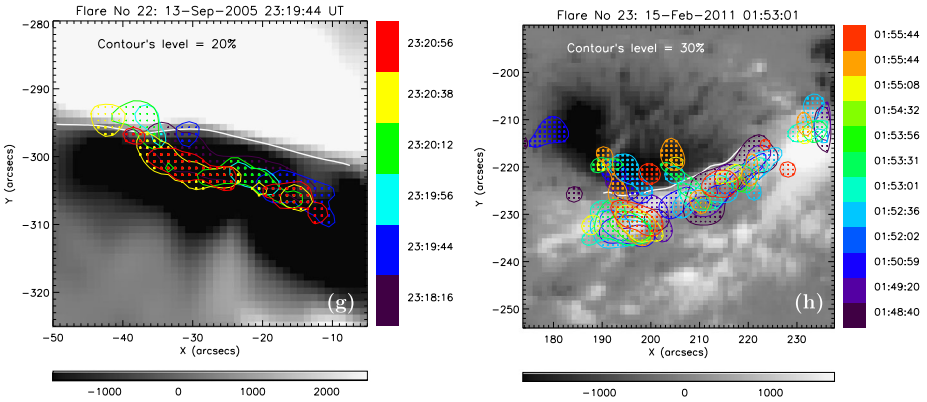


**Figure 17** (*Continued.*)

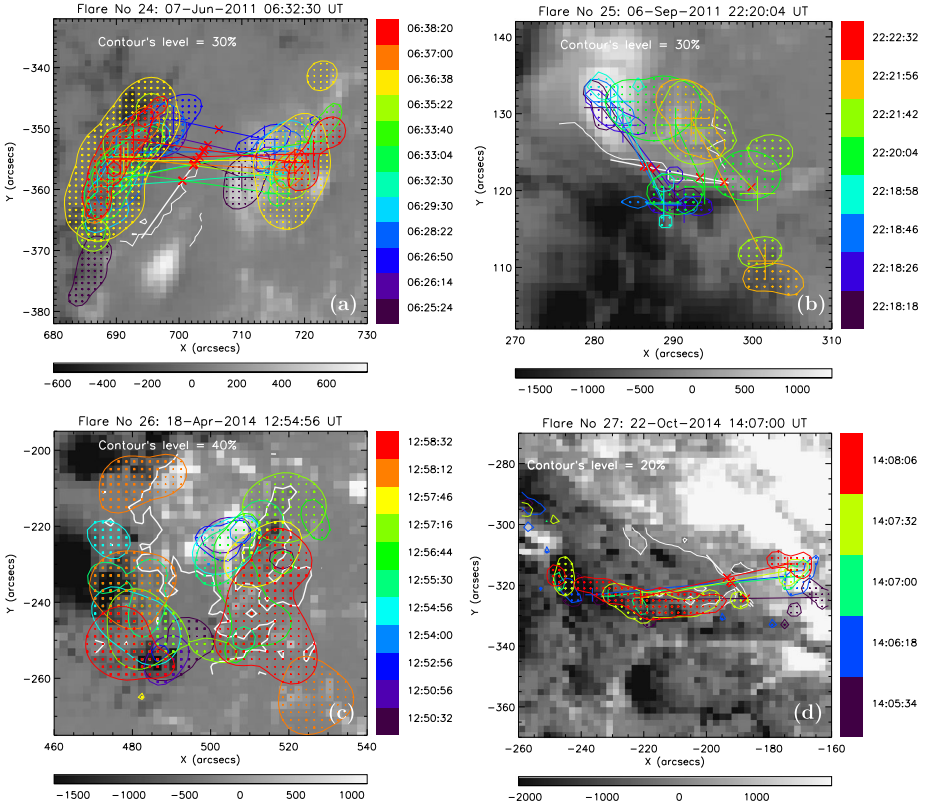


**Figure 18** Spatio-temporal evolution of the sources of the HXR pulsations in flares No. 24 – 29. The method and convention are the same as in Figure 15.

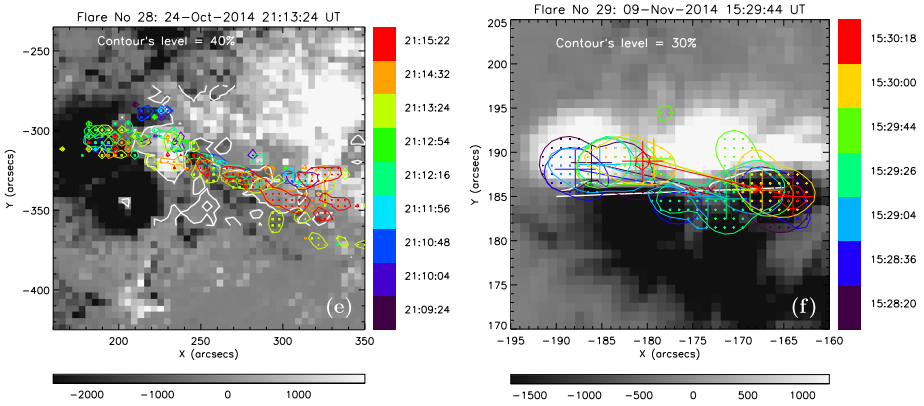


**Figure 18** (*Continued.*)

## References


Artemyev, A., Zimovets, I.: 2012, Stability of current sheets in the solar corona. *Solar Phys.* **277**, 283. DOI. ADS.

Aschwanden, M.J.: 1987, Theory of radio pulsations in coronal loops. *Solar Phys.* **111**, 113. DOI. ADS.

Aschwanden, M.J.: 2002, Particle acceleration and kinematics in solar flares – A synthesis of recent observations and theoretical concepts (Invited Review). *Space Sci. Rev.* **101**, 1. DOI. ADS.

Aschwanden, M.J., Schwartz, R.A., Alt, D.M.: 1995, Electron time-of-flight differences in solar flares. *Astrophys. J.* **447**, 923. DOI. ADS.

Aschwanden, M.J., Kliem, B., Schwarz, U., Kurths, J., Dennis, B.R., Schwartz, R.A.: 1998, Wavelet analysis of solar flare hard X-rays. *Astrophys. J.* **505**, 941. DOI. ADS.

Aulanier, G., Pariat, E., Démoulin, P., DeVore, C.R.: 2006, Slip-running reconnection in quasi-separatrix layers. *Solar Phys.* **238**, 347. DOI. ADS.

Bogachev, S.A., Somov, B.V., Kosugi, T., Sakao, T.: 2005, The motions of the hard X-ray sources in solar flares: Images and statistics. *Astrophys. J.* **630**, 561. DOI. ADS.

Brown, J.C., Hoyng, P.: 1975, Betatron acceleration in a large solar hard X-ray burst. *Astrophys. J.* **200**, 734. DOI. ADS.

de Jager, C.: 1979, On the seats of elementary flare bursts. *Solar Phys.* **64**, 135. DOI. ADS.

de Jager, C., de Jonge, G.: 1978, Properties of elementary flare bursts. *Solar Phys.* **58**, 127. DOI. ADS.

Dennis, B.R.: 1988, Solar flare hard X-ray observations. *Solar Phys.* **118**, 49. DOI. ADS.

Dolla, L., Marqué, C., Seaton, D.B., Van Doorsselaere, T., Dominique, M., Berghmans, D., Cabanas, C., De Groof, A., Schmutz, W., Verdini, A., West, M.J., Zender, J., Zhukov, A.N.: 2012, Time delays in quasi-periodic pulsations observed during the X2.2 solar flare on 2011 February 15. *Astrophys. J. Lett.* **749**, L16. DOI. ADS.

Dudík, J., Janvier, M., Aulanier, G., Del Zanna, G., Karlický, M., Mason, H.E., Schmieder, B.: 2014, Slipping magnetic reconnection during an X-class solar flare observed by SDO/AIA. *Astrophys. J.* **784**, 144. DOI. ADS.

Emslie, A.G.: 1981, An interacting loop model for solar flare bursts. *Astrophys. Lett.* **22**, 171. ADS.

Fletcher, L., Hudson, H.S.: 2002, Spectral and spatial variations of flare hard X-ray footpoints. *Solar Phys.* **210**, 307. DOI. ADS.

Foullon, C., Verwichte, E., Nakariakov, V.M., Fletcher, L.: 2005, X-ray quasi-periodic pulsations in solar flares as magnetohydrodynamic oscillations. *Astron. Astrophys.* **440**, L59. DOI. ADS.

Gan, W.Q., Li, Y.P., Miroshnichenko, L.I.: 2008, On the motions of RHESSI flare footpoints. *Adv. Space Res.* **41**, 908. DOI. ADS.

Goddard, C.R., Nisticò, G., Nakariakov, V.M., Zimovets, I.V.: 2016, A statistical study of decaying kink oscillations detected using SDO/AIA. *Astron. Astrophys.* **585**, A137. DOI. ADS.

Grigis, P.C., Benz, A.O.: 2005, The evolution of reconnection along an arcade of magnetic loops. *Astrophys. J. Lett.* **625**, L143. DOI. ADS.

Gruber, D., Lachowicz, P., Bissaldi, E., Briggs, M.S., Connaughton, V., Greiner, J., van der Horst, A.J., Kanbach, G., Rau, A., Bhat, P.N., Diehl, R., von Kienlin, A., Kippen, R.M., Meegan, C.A., Paciesas,

W.S., Preece, R.D., Wilson-Hodge, C.: 2011, Quasi-periodic pulsations in solar flares: New clues from the Fermi gamma-ray burst monitor. *Astron. Astrophys.* **533**, A61. DOI. ADS.
Hood, A.W., Cargill, P.J., Browning, P.K., Tam, K.V.: 2016, An MHD avalanche in a multi-threaded coronal loop. *Astrophys. J.* **817**, 5. DOI. ADS.
Hurford, G.J., Schmahl, E.J., Schwartz, R.A., Conway, A.J., Aschwanden, M.J., Csillaghy, A., Dennis, B.R., Johns-Krull, C., Krucker, S., Lin, R.P., McTiernan, J., Metcalf, T.R., Sato, J., Smith, D.M.: 2002, The RHESSI imaging concept. *Solar Phys.* **210**, 61. DOI. ADS.
Inglis, A.R., Dennis, B.R.: 2012, The relationship between hard X-ray pulse timings and the locations of footpoint sources during solar flares. *Astrophys. J.* **748**, 139. DOI. ADS.
Inglis, A.R., Gilbert, H.R.: 2013, Hard X-ray and ultraviolet emission during the 2011 June 7 solar flare. *Astrophys. J.* **777**, 30. DOI. ADS.
Inglis, A.R., Ireland, J., Dominique, M.: 2015, Quasi-periodic pulsations in solar and stellar flares: Re-evaluating their nature in the context of power-law flare Fourier spectra. *Astrophys. J.* **798**, 108. DOI. ADS.
Jakimiec, J., Tomczak, M.: 2013, Quasi-periodic variations in the hard X-ray emission of a large arcade flare. *Solar Phys.* **286**, 427. DOI. ADS.
Jakimiec, J., Tomczak, M.: 2014, Investigation of the X-ray emission of the large arcade flare of 2 March 1993. *Solar Phys.* **289**, 2073 DOI. ADS.
Janvier, M., Aulanier, G., Pariat, E., Démoulin, P.: 2013, The standard flare model in three dimensions. III. Slip-running reconnection properties. *Astron. Astrophys.* **555**, A77. DOI. ADS.
Ji, H., Huang, G., Wang, H., Zhou, T., Li, Y., Zhang, Y., Song, M.: 2006, Converging motion of H$\alpha$ conjugate kernels: The signature of fast relaxation of a sheared magnetic field. *Astrophys. J. Lett.* **636**, L173. DOI. ADS.
Kliem, B., Karlický, M., Benz, A.O.: 2000, Solar flare radio pulsations as a signature of dynamic magnetic reconnection. *Astron. Astrophys.* **360**, 715. ADS.
Kosugi, T., Makishima, K., Murakami, T., Sakao, T., Dotani, T., Inda, M., Kai, K., Masuda, S., Nakajima, H., Ogawara, Y., Sawa, M., Shibasaki, K.: 1991, The Hard X-ray Telescope (HXT) for the SOLAR-A mission. *Solar Phys.* **136**, 17. DOI. ADS.
Krucker, S., Hurford, G.J., Lin, R.P.: 2003, Hard X-ray source motions in the 2002 July 23 gamma-ray flare. *Astrophys. J. Lett.* **595**, L103. DOI. ADS.
Kupriyanova, E.G., Melnikov, V.F., Nakariakov, V.M., Shibasaki, K.: 2010, Types of microwave quasi-periodic pulsations in single flaring loops. *Solar Phys.* **267**, 329. DOI. ADS.
Li, Y.P., Gan, W.Q.: 2008, Observational studies of the X-ray quasi-periodic oscillations of a solar flare. *Solar Phys.* **247**, 77. DOI. ADS.
Li, D., Ning, Z.J., Zhang, Q.M.: 2015, Imaging and spectral observations of quasi-periodic pulsations in a solar flare. *Astrophys. J.* **807**, 72. DOI. ADS.
Li, T., Zhang, J.: 2015, Quasi-periodic slipping magnetic reconnection during an X-class solar flare observed by the solar dynamics observatory and interface region imaging spectrograph. *Astrophys. J. Lett.* **804**, L8. DOI. ADS.
Lin, R.P., Dennis, B.R., Hurford, G.J., Smith, D.M., Zehnder, A., Harvey, P.R., Curtis, D.W., Pankow, D., Turin, P., Bester, M., Csillaghy, A., Lewis, M., Madden, N., van Beek, H.F., Appleby, M., Raudorf, T., McTiernan, J., Ramaty, R., Schmahl, E., Schwartz, R., Krucker, S., Abiad, R., Quinn, T., Berg, P., Hashii, M., Sterling, R., Jackson, R., Pratt, R., Campbell, R.D., Malone, D., Landis, D., Barrington-Leigh, C.P., Slassi-Sennou, S., Cork, C., Clark, D., Amato, D., Orwig, L., Boyle, R., Banks, I.S., Shirey, K., Tolbert, A.K., Zarro, D., Snow, F., Thomsen, K., Henneck, R., McHedlishvili, A., Ming, P., Fivian, M., Jordan, J., Wanner, R., Crubb, J., Preble, J., Matranga, M., Benz, A., Hudson, H., Canfield, R.C., Holman, G.D., Crannell, C., Kosugi, T., Emslie, A.G., Vilmer, N., Brown, J.C., Johns-Krull, C., Aschwanden, M., Metcalf, T., Conway, A.: 2002, The Reuven Ramaty High-Energy Solar Spectroscopic Imager (RHESSI). *Solar Phys.* **210**, 3. DOI. ADS.
Liu, R., Alexander, D., Gilbert, H.R.: 2009, Asymmetric eruptive filaments. *Astrophys. J.* **691**, 1079. DOI. ADS.
McAteer, R.T.J., Young, C.A., Ireland, J., Gallagher, P.T.: 2007, The bursty nature of solar flare X-ray emission. *Astrophys. J.* **662**, 691. DOI. ADS.
McLaughlin, J.A., Thurgood, J.O., MacTaggart, D.: 2012, On the periodicity of oscillatory reconnection. *Astron. Astrophys.* **548**, A98. DOI. ADS.
Nakariakov, V.M., Melnikov, V.F.: 2009, Quasi-periodic pulsations in solar flares. *Space Sci. Rev.* **149**, 119. DOI. ADS.
Nakariakov, V.M., Verwichte, E.: 2005, Coronal waves and oscillations. *Living Rev. Solar Phys.* **2**. DOI. ADS.
Nakariakov, V.M., Zimovets, I.V.: 2011, Slow magnetoacoustic waves in two-ribbon flares. *Astrophys. J. Lett.* **730**, L27. DOI. ADS.

Nakariakov, V.M., Foullon, C., Verwichte, E., Young, N.P.: 2006, Quasi-periodic modulation of solar and stellar flaring emission by magnetohydrodynamic oscillations in a nearby loop. *Astron. Astrophys.* **452**, 343. DOI. ADS.

Nakariakov, V.M., Inglis, A.R., Zimovets, I.V., Foullon, C., Verwichte, E., Sych, R., Myagkova, I.N.: 2010, Oscillatory processes in solar flares. *Plasma Phys. Control. Fusion* **52**(12), 124009. DOI. ADS.

Nakariakov, V.M., Pilipenko, V., Heilig, B., Jelinek, P., Karlicky, M., Klimushkin, D.Y., Kolotkov, D.Y., Lee, D.-H., Nistico, G., Van Doorsselaere, T., Verth, G., Zimovets, I.V.: 2016, Magnetohydrodynamic oscillations in the solar corona and Earth's magnetosphere: Towards consolidated understanding. *Space Sci. Rev.* **1**. DOI.

Nordlund, Å., Stein, R.F., Asplund, M.: 2009, Solar surface convection. *Living Rev. Solar Phys.* **6**. DOI. ADS.

Ofman, L., Sui, L.: 2006, Oscillations of hard X-ray flare emission observed by RHESSI: Effects of super-Alfvénic beams? *Astrophys. J. Lett.* **644**, L149. DOI. ADS.

Priest, E.R., Démoulin, P.: 1995, Three-dimensional magnetic reconnection without null points. 1. Basic theory of magnetic flipping. *J. Geophys. Res.* **100**, 23443. DOI. ADS.

Priest, E.R., Forbes, T.G.: 2002, The magnetic nature of solar flares. *Astron. Astrophys. Rev.* **10**, 313. DOI. ADS.

Sakao, T., Kosugi, T., Masuda, S.: 1998, Energy release and particle acceleration in solar flares with respect to flaring magnetic loops. In: Watanabe, T., Kosugi, T. (eds.) *Observational Plasma Astrophysics: Five Years of YOHKOH and Beyond*, *Astrophysics and Space Science Library* **229**, 273. DOI. ADS.

Scherrer, P.H., Bogart, R.S., Bush, R.I., Hoeksema, J.T., Kosovichev, A.G., Schou, J., Rosenberg, W., Springer, L., Tarbell, T.D., Title, A., Wolfson, C.J., Zayer, I. (MDI Engineering Team): 1995, The solar oscillations investigation – Michelson Doppler imager. *Solar Phys.* **162**, 129. DOI. ADS.

Scherrer, P.H., Schou, J., Bush, R.I., Kosovichev, A.G., Bogart, R.S., Hoeksema, J.T., Liu, Y., Duvall, T.L., Zhao, J., Title, A.M., Schrijver, C.J., Tarbell, T.D., Tomczyk, S.: 2012, The Helioseismic and Magnetic Imager (HMI) investigation for the Solar Dynamics Observatory (SDO). *Solar Phys.* **275**, 207. DOI. ADS.

Schmieder, B., Démoulin, P., Aulanier, G.: 2013, Solar filament eruptions and their physical role in triggering coronal mass ejections. *Adv. Space Res.* **51**, 1967. DOI. ADS.

Schrijver, C.J.: 2009, Driving major solar flares and eruptions: A review. *Adv. Space Res.* **43**, 739. DOI. ADS.

Shibata, K., Magara, T.: 2011, Solar flares: Magnetohydrodynamic processes. *Living Rev. Solar Phys.* **8**. DOI. ADS.

Simões, P.J.A., Hudson, H.S., Fletcher, L.: 2015, Soft X-ray pulsations in solar flares. *Solar Phys.* **290**, 3625. DOI. ADS.

Simões, P.J.A., Fletcher, L., Hudson, H.S., Russell, A.J.B.: 2013, Implosion of coronal loops during the impulsive phase of a solar flare. *Astrophys. J.* **777**, 152. DOI. ADS.

Somov, B.V.: 2007, *Plasma Astrophysics, Part II: Reconnection and Flares*. ADS.

Sych, R., Nakariakov, V.M., Karlicky, M., Anfinogentov, S.: 2009, Relationship between wave processes in sunspots and quasi-periodic pulsations in active region flares. *Astron. Astrophys.* **505**, 791. DOI. ADS.

Tajima, T., Sakai, J., Nakajima, H., Kosugi, T., Brunel, F., Kundu, M.R.: 1987, Current loop coalescence model of solar flares. *Astrophys. J.* **321**, 1031. DOI. ADS.

Torrence, C., Compo, G.P.: 1998, A practical guide to wavelet analysis. *Bull. Am. Meteorol. Soc.* **79**, 61. DOI. ADS.

van Beek, H.F., de Feiter, L.D., de Jager, C.: 1974a, Hard X-ray observations of elementary flare bursts, and their interpretation. In: Rycroft, M.J., Reasenberg, R.D. (eds.) *Space Research XIV*, 447. ADS.

van Beek, H.F., de Feiter, L.D., de Jager, C.: 1974b, Time profiles and photon spectra of solar hard X-rays. In: Page, D.E. (ed.) *Correlated Interplanetary and Magnetospheric Observations*, *Astrophysics and Space Science Library* **42**, 533. DOI. ADS.

Vaughan, S.: 2005, A simple test for periodic signals in red noise. *Astron. Astrophys.* **431**, 391. DOI. ADS.

Veronig, A.M., Brown, J.C.: 2004, A coronal thick-target interpretation of two hard X-ray loop events. *Astrophys. J. Lett.* **603**, L117. DOI. ADS.

White, S.M., Benz, A.O., Christe, S., Fárník, F., Kundu, M.R., Mann, G., Ning, Z., Raulin, J.-P., Silva-Válio, A.V.R., Saint-Hilaire, P., Vilmer, N., Warmuth, A.: 2011, The relationship between solar radio and hard X-ray emission. *Space Sci. Rev.* **159**, 225. DOI. ADS.

Yang, Y.-H., Cheng, C.Z., Krucker, S., Lin, R.P., Ip, W.H.: 2009, A statistical study of hard X-ray footpoint motions in large solar flares. *Astrophys. J.* **693**, 132. DOI. ADS.

Zaitsev, V.V., Stepanov, A.V.: 1982, On the origin of the hard X-ray pulsations during solar flares. *Sov. Astron. Lett.* **8**, 132. ADS.

Zaitsev, V.V., Stepanov, A.V.: 2008, Reviews of topical problems: Coronal magnetic loops. *Phys. Usp.* **51**, 1123. DOI. ADS.

Zimovets, I.V., Kuznetsov, S.A., Struminsky, A.B.: 2013, Fine structure of the sources of quasi-periodic pulsations in "single-loop" solar flares. *Astron. Lett.* **39**, 267. DOI. ADS.
Zimovets, I.V., Struminsky, A.B.: 2009, Imaging observations of quasi-periodic pulsatory nonthermal emission in two-ribbon solar flares. *Solar Phys.* **258**, 69. DOI. ADS.
Zimovets, I.V., Struminsky, A.B.: 2010, Observations of double-periodic X-ray emission in interacting systems of solar flare loops. *Solar Phys.* **263**, 163. DOI. ADS.